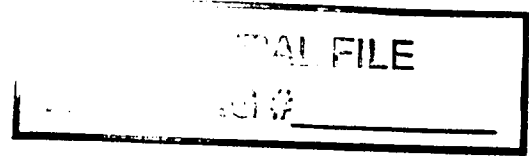


XAA-0075/TE



EFFECT OF SOUND ON BOUNDARY LAYER STABILITY

by

William S. Saric and Shelly Anne Spencer

Arizona State University
Tempe, AZ

1017-1017-1017

Final report submitted to NASA Ames Research Center
Cooperative Agreement NCC2-659

June 1993

JUN 14 1996

CASI

CENTRAL OFFICE FILE

ABSTRACT

Experiments are conducted in the Arizona State University Unsteady Wind Tunnel with a zero-pressure-gradient flat-plate model that has a 67:1 elliptical leading edge. Boundary-layer measurements are made of the streamwise fluctuating-velocity component in order to identify the amplified T-S waves that are forced by downstream-travelling sound waves. Measurements are taken with circular 3-D roughness elements placed at the Branch I neutral stability point for the frequency under consideration, and then with the roughness element downstream of Branch I. These roughness elements have a principal chord dimension equal to $2\lambda_{TS}/\pi$ of the T-S waves under study and are “stacked” in order to resemble a Gaussian height distribution. Measurements taken just downstream of the roughness (with leading-edge T-S waves, surface roughness T-S waves, instrumentation sting vibrations and the Stokes wave subtracted) show the generation of 3-D T-S waves, but not in the characteristic heart-shaped disturbance field predicted by 3-D asymptotic theory. Maximum disturbance amplitudes are found on the roughness centerline. However, some near-field characteristics predicted by numerical modelling are observed.

ACKNOWLEDGEMENTS

Work by Shelly Spencer was supported by NASA, Ames Research Center, Cooperative Agreement NCC2-659. The time of the Principal Investigator William Saric, and the wind tunnel staff was supported by the Air Force Office of Scientific Research Grant AFOSR-90-0234.

TABLE OF CONTENTS

	Page
LIST OF TABLES	viii
LIST OF FIGURES	ix
NOMENCLATURE	xii
CHAPTER I INTRODUCTION	1
1.1. Boundary-Layer Stability	1
1.1.1. Tollmien-Schlichting Instability Waves	1
1.1.2. Boundary-Layer Receptivity	3
1.1.3. Transition Control	4
1.2. Experimental and Theoretical Review	4
1.2.1. Freestream Turbulence	5
1.2.2. Leading-Edge Receptivity	6
1.2.3. Receptivity to 2-D Disturbances	7
1.2.4. Receptivity to 3-D Disturbances	11
1.3. Experiment Objectives	13
CHAPTER II THEORY	16
2.1. Three-Dimensional Stability Theory	16
2.2. Three-Dimensional Stability Computations	19
2.3. Experimental Deviations from Theory	21

	Page
CHAPTER III EXPERIMENTAL FACILITY AND EQUIPMENT	22
3.1. Sound System	22
3.2. Roughness Specifications	23
3.3. Freestream Control	23
3.4. Signal-Analysis Equipment	24
CHAPTER IV EXPERIMENTAL TECHNIQUES	26
4.1. Scaling the Experiment	26
4.2. Roughness-Signal Discrimination	29
4.3. Three-Dimensional Disturbance Mapping	32
CHAPTER V DATA ACQUISITION	34
5.1. Preparation and Calibration	34
5.2. Sample Data	35
5.3. Codes	36
CHAPTER VI RESULTS	40
6.1. 3-D Roughness at Branch I	40
6.1.1. Spanwise and Streamwise Variation of u'	41
6.1.2. Spanwise and Normal Variation of u'	42
6.2. 3-D Roughness Downstream of Branch I	43
6.2.1. Spanwise and Streamwise Variation of u'	43
6.2.2. Spanwise and Normal Variation of u'	44
6.3. Comparison with Numerical Model	45

	Page
CHAPTER VII CONCLUSIONS	48
REFERENCES	50
APPENDIX A FACILITY	54

LIST OF TABLES

Table		Page
1	Freestream Turbulence Levels	56
2	Traverse Specifications	57

LIST OF FIGURES

Figure	Page
2.1 Triple-deck structure.	58
2.2 3-D roughness disturbance-field characteristics.	59
2.3 3-D roughness element.	60
2.4 Comparison of 3-D roughness and Gaussian distribution.	61
3.1 ASU Unsteady Wind Tunnel.	62
3.2 Speaker location in wind tunnel.	63
4.1 Amplitudes of acoustic and noise signals: freestream hot-wire.	64
4.2 Amplitudes of acoustic and noise signals: boundary-layer hot-wire.	65
4.3 Direct measurement of Stokes layer compared with theoretical profile.	66
4.4 Complex plane signal subtraction technique.	67
4.5 Roughness signal discrimination technique applied to 2-D T-S wave.	68
4.6 Example of 3-D roughness T-S signal discrimination.	69
4.7 Measurement locations: 3-D roughness at Branch I.	70
4.8 Measurement locations: 3-D roughness downstream of Branch I.	71
6.1 Spanwise and streamwise variation of u' amplitude: 3-D roughness element at Branch I; $x = D$ to $x = 3D$; $U(y) = 0.47$; $SPL = 93$ dB.	72

Figure		Page
6.2	Spanwise and streamwise variation of u' phase: 3-D roughness element at Branch I; $x = D$ to $x = 3D$; $U(y) = 0.47$; $SPL = 93$ dB.	73
6.3	Spanwise and streamwise variation of u' amplitude: 3-D roughness element at Branch I; $x = 3D$ to $x = 12D$; $U(y) = 0.47$; $SPL = 93$ dB.	74
6.4	Spanwise and streamwise variation of u' phase: 3-D roughness element at Branch I; $x = 3D$ to $x = 12D$; $U(y) = 0.47$; $SPL = 93$ dB.	75
6.5	Spanwise and normal variation of u' amplitude: 3-D roughness element at Branch I; $z = -D$ to $z = D$; $x = 2.5D$; $SPL = 93$ dB.	76
6.6	Spanwise and normal variation of u' phase: 3-D roughness element at Branch I; $z = -D$ to $z = D$; $x = 2.5D$; $SPL = 93$ dB.	77
6.7	Spanwise and normal variation of u' amplitude: 3-D roughness element at Branch I; $z = -1.25D$ to $z = 0$; $x = 2.5D$; $SPL = 93$ dB.	78
6.8	Spanwise and normal variation of u' phase: 3-D roughness element at Branch I; $z = -1.25D$ to $z = 0$; $x = 2.5D$; $SPL = 93$ dB.	79
6.9	Spanwise and streamwise variation of u' amplitude: 3-D roughness element $12D$ downstream of Branch I; $x = 1.5D$ to $x = 3.5D$; $U(y) = 0.40$; $SPL = 93$ dB.	80
6.10	Spanwise and streamwise variation of u' phase: 3-D roughness element $12D$ downstream of Branch I; $x = 1.5D$ to $x = 3.5D$; $U(y) = 0.40$; $SPL = 93$ dB.	81
6.11	Spanwise and streamwise variation of u' amplitude: 3-D roughness element $12D$ downstream of Branch I; $x = 1.5D$ to $x = 3.5D$; $U(y) = 0.40$; $SPL = 95$ dB.	82

Figure		Page
6.12	Spanwise and streamwise variation of u' phase: 3-D roughness element $12D$ downstream of Branch I; $x = 1.5D$ to $x = 3.5D$; $U(y) = 0.40$; $SPL = 95$ dB.	83
6.13	Spanwise and normal variation of u' amplitude: 3-D roughness element $12D$ downstream of Branch I; $z = -1.25D$ to $z = 0$; $x = 2.5D$; $SPL = 93$ dB.	84
6.14	Spanwise and normal variation of u' phase: 3-D roughness element $12D$ downstream of Branch I; $z = -1.25D$ to $z = 0$; $x = 2.5D$; $SPL = 93$ dB.	85
6.15	Spanwise and normal variation of u' amplitude: 3-D roughness element $12D$ downstream of Branch I; $z = -1.25D$ to $z = 0$; $x = 2.5D$; $SPL = 95$ dB.	86
6.16	Spanwise and normal variation of u' phase: 3-D roughness element $12D$ downstream of Branch I; $z = -1.25D$ to $z = 0$; $x = 2.5D$; $SPL = 95$ dB.	87
6.17	Streamwise and spanwise variation of disturbance-velocity amplitude: $S_o = 2.0$, $Y_r = 1.0$	88
6.18	Streamwise and normal variation of u' amplitude: $S_o = 2.0$, $Y_r = 1.0$, $z = 0$	89
6.19	Streamwise and spanwise variation of disturbance-velocity amplitude: $S_o = 3.0$, $Y_r = 1.0$	90
6.20	Streamwise and normal variation of u' amplitude: $S_o = 3.0$, $Y_r = 1.0$, $z = 0$	91

NOMENCLATURE

c	speed of sound [m/s]
D	3-D roughness diameter [m]
F	$= 2\pi\nu f/U_\infty^2$, dimensionless frequency
f	frequency [Hz]
h	3-D roughness height [m]
H	maximum 3-D roughness height [m]
k_r	real part of wavenumber vector
p'	disturbance-state pressure
r	3-D roughness radius [m]
R	$= (R_x)^{1/2} = U_\infty \delta_r / \nu$, boundary-layer Reynolds number
R_x	$= U_\infty x^* / \nu$, x -Reynolds number
s	$= \epsilon^2 S = (R_x)^{3/4} F$, dimensionless frequency
S	$= \omega^* x^* / U_\infty$, Strouhal number
S_o	$= \lambda^{-3/2} \epsilon^2 S$, scaled Strouhal number
U	basic-state chordwise boundary-layer velocity normalized by U_∞
U_∞	freestream velocity [m/s]
u', v', w'	disturbance velocity field normalized by U_∞
$ u' $	rms of u'
x, z	chordwise and spanwise coordinates scaled by D , measured from the roughness element center

x^*, y^*, z^*	chordwise (measured from x_v^*), normal, and spanwise coordinates [m]
x_v^*	virtual leading edge
Y	$= y^*/(\epsilon^5 x^*)$, lower viscous deck scaling variable
Y_r	$= H/(\epsilon^5 x^*)$, maximum height of roughness element in lower viscous deck
δ_r	$= (\nu x^*/U_\infty)^{1/2}$, boundary-layer reference length [m]
ϵ	$= R^{-1/4}$, small scaling variable
η	$= y^*/\delta_r$, boundary-layer normal-to-the-surface coordinate
λ	slope of Blasius boundary layer near the surface
λ_{TS}	T-S wavelength [m]
λ_{ac}	acoustic wavelength [m]
ν	kinematic viscosity [m ² /s]
ρ	density [kg/m ³]
ω^*	frequency [rad]

CHAPTER I

INTRODUCTION

Since the pivotal Schubauer and Skramstad experiments (1947a,b), much progress has been made toward understanding the instabilities which cause boundary-layer transition. Despite the continuous efforts of experimentalists and theorists, more research will be necessary before the causes and exact roles of these instabilities are fully understood. Linear stability theory and its extension to nonparallel boundary layers very closely predicts the effect of a disturbance in the boundary layer, but the question of reasonable initial conditions remains difficult in experiments. The present challenge is in identifying the mechanism by which freestream disturbances are transmitted into the boundary layer and then quantifying the effect of a given “receptivity mechanism”.

1.1. Boundary-Layer Stability

The development of viscous stability theory has been an interesting chapter in the science of fluid dynamics. It is one of the few disciplines in which a theory was developed without experimental evidence and later verified through testing.

1.1.1. Tollmien-Schlichting Instability Waves

At Göttingen, Prandtl (1928) examined the effect of a sinusoidal disturbance on a viscous boundary layer. This was the first published explanation of a viscous instability mechanism. Before this time, inviscid stability theory predicted stability for a flat-plate

boundary layer. Prandtl's analysis was not well received, largely due to a lack of experimental evidence. Scientists were reluctant to believe that a theory which predicted stability in the inviscid limit would counter-intuitively lead to instability when a small amount of viscosity was taken into account. However, the concept was reinforced when Tollmien (1931) presented an asymptotic viscous stability theory for a Blasius boundary layer, and Schlichting (1933, 1935) calculated part of the neutral stability curve. Still, not until 1943 was the theory validated by experiment.

At the National Bureau of Standards, with the support of Hugh Dryden, Schubauer and Skramstad built a low-turbulence wind tunnel and conducted experiments to investigate laminar boundary-layer oscillations and transition on a flat plate. The instability waves found corresponded with those predicted by asymptotic viscous stability theory. The following passage from Schubauer and Skramstad's published results (1947a), after declassification of the work, shows even the experimenters' surprise at their success.

When these experiments were being performed, each check with theory was a stimulating experience. There was nothing so unusual about setting up a wavy disturbance in the boundary layer, but finding that this waviness really constituted a unique wave phenomenon with properties determined by the boundary-layer flow was out of the ordinary.

Schubauer and Skramstad's experiments removed all doubt from the basic validity of viscous stability theory. The new question raised was how the instability waves originated in the boundary layer.

1.1.2. Boundary-Layer Receptivity

“Receptivity” is the term used to describe the mechanism by which freestream disturbances enter the boundary layer and generate unstable waves (Morkovin, 1969). Examples of receptors in a flat-plate boundary layer include leading-edge curvature, the leading-edge juncture with the plate, surface roughness elements, and suction or blowing. Indeed, any surface inhomogeneity or mechanism causing short-length-scale, localized pressure gradients in the boundary layer has the potential to entrain freestream disturbances and act as a receptivity mechanism (Nishioka & Morkovin, 1986).

Identifying and quantifying all sources of boundary-layer receptivity is a challenging task. Most receptivity experiments attempt to carefully control the environment and limit the study to one receptivity mechanism, often designed to excite T-S waves at a particular frequency in a Blasius boundary-layer. Freestream disturbances may be introduced via acoustic waves or convected gusts. Another common approach is to bypass the receptivity mechanism and initiate the disturbance directly in the boundary layer to examine the development and effects of the unstable waves generated. This may be accomplished with a vibrating ribbon or pulsed or harmonic acoustic source within the boundary layer.

Experiments involving receptivity to freestream sound must be approached cautiously. Nishioka and Morkovin (1986) point out several common problems with past experiments which should be avoided. Often the acoustic field outside the boundary layer is not sufficiently documented, including any standing waves and the forcing field at the boundary layer’s edge. Also, freestream disturbance amplitudes should be limited to maintain

linearity of the forcing field, and any vibration of the leading edge should be noted. Within the boundary layer, the effect of the forcing should be fully documented. Additionally, it is important that freestream turbulence levels are very low, that as little receptivity as possible is provided by the model leading edge, and that surface roughness is minimized, since all of these factors contribute to boundary-layer receptivity (Saric, 1990).

1.1.3. Transition Control

While the experiments associated with boundary-layer receptivity may be tedious, the rewards to be gained from understanding the mechanisms are significant. Simply being able to accurately predict the transition location on an airplane wing would be an accomplishment. If the mechanisms which cause transition are correctly identified, the control of transition becomes an intriguing possibility. Delayed transition decreases skin-friction drag while early transition may be desirable to maintain boundary-layer attachment.

The field of Laminar Flow Control (LFC) examines the effect of devices such as suction slots near a wing leading edge to limit growth of disturbances in the boundary layer and delay transition. Another approach in transition control involves creation of T-S instability waves (using applied surface roughness, for example) designed to interfere with existing T-S waves from the leading edge or surface roughness. Cancellation or amplification from superposition of the instability waves is possible using this technique.

1.2. Experimental and Theoretical Review

The following is a summary of relevant receptivity experiments conducted on a Blasius boundary layer. Discussion of some theoretical and computational results is also given, but

the emphasis is experimental. Included are effects of freestream turbulence, leading-edge curvature and juncture, two-dimensional (2-D) disturbances, and three-dimensional (3-D) disturbances with forcing provided by freestream sound or vortical disturbances.

1.2.1. Freestream Turbulence

Freestream disturbances provide the perturbation necessary to instigate Blasius boundary-layer instability. In order to determine the physical mechanism by which this occurs and to quantify the forcing and response amplitudes, it is desirable to have a known freestream disturbance. This is generally accomplished by performing boundary-layer stability measurements in a low-turbulence environment, and then introducing a known disturbance via freestream sound waves, convected periodic gusts or vortical disturbances.

Care must be taken when measuring natural freestream turbulence levels in a wind tunnel. It is important to cite both disturbance amplitudes and the frequency range of the signal filtering (Saric, Takagi, & Mousseux, 1988). Long-wavelength freestream disturbances are frequently modelled using acoustic waves. A relatively new technique for introducing freestream disturbances is the generation of periodic gusts using an oscillating ribbon array (Parekh, Pulvin, & Wlezien, 1991). The disturbance created by the oscillating array resembles a sinusoidal wake and is generated at a single wave number.

Recent freestream turbulence experiments by Kendall (1985, 1990) emphasize the need for a well-known disturbance field. Kendall used a grid to create freestream turbulence and in one instance found that streamwise vortical disturbances created by the grid were ingested into the boundary layer. In that case, T-S wave instability was dominated by the

streamwise vorticity in the boundary layer. At lower levels of freestream turbulence, when the T-S instability dominated, the amplitudes of the T-S waves were found to increase nonlinearly with amplitudes of freestream turbulence. One concludes that relatively low levels of freestream disturbances are required for receptivity experiments.

1.2.2. Leading-Edge Receptivity

Acoustic receptivity at the leading edge of a flat-plate model can occur for two reasons: from curvature of the leading edge and from the juncture between the leading edge and flat plate. (The juncture acts as a 2-D disturbance and will be discussed in the following section.) Goldstein (1983) presents the theoretical mechanism by which long-wavelength freestream disturbances are transformed to short-wavelength T-S waves due to the leading-edge curvature. The conversion takes place in the overlap region where the unsteady boundary-layer equations governing at the leading edge join the Orr-Sommerfeld solution governing on the flat plate. The method of matched asymptotic expansions is used to match boundary conditions here, and this matching provides the proper length scales for the wavelength conversion to take place. Goldstein, Sockol, and Sanz (1983) additionally computed matching coefficients in support of this theory. More recently, Kerschen extends this theory to include leading-edge receptivity of a flat plate in a channel to acoustic waves and leading-edge receptivity to convected gusts (1989).

Several attempts have been made to numerically model leading-edge curvature receptivity to acoustic waves, but only the most recent from Lin, Reed, and Saric (1991) includes a non-zero flat-plate thickness. Lin, et al., solve the full Navier-Stokes equations in general

curvilinear coordinates using a finite-difference method which is second-order accurate in time and space. Less receptivity is detected from larger aspect ratio elliptic leading edges, and smoothing the leading-edge juncture is found to decrease receptivity. A super ellipse configuration, with no curvature discontinuity at the juncture, is also examined.

The receptivity experiments of Wlezien (1989) and Wlezien, Parekh, and Island (1990), used elliptic leading edges with aspect ratios of 6:1 and 24:1. It was noted that significantly less leading-edge receptivity was observed from the 24:1 ellipse for the case of acoustic freestream disturbances. Parekh, Pulvin, and Wlezien (1991) examined leading-edge receptivity to convected gusts. For a gust incidence angle of zero degrees, parallel with the flat-plate leading edge, no T-S response was detected. However, future experiments are planned for nonzero gust incidence angle, which theoretically should produce a larger T-S response. It should be noted that T-S waves generated by leading-edge curvature have more time to decay before reaching the neutral stability location than T-S waves generated by a leading-edge juncture. Therefore, the latter are often found to be more significant in receptivity experiments.

1.2.3. Receptivity to 2-D Disturbances

The amplitudes of unstable T-S waves predicted by leading-edge curvature theory are often not large enough to explain the measurements of T-S waves downstream of leading-edge regions in experiments. This was noted by Goldstein (1985) when comparing his 1983 computations to the leading-edge receptivity experiments of Leehey and Shapiro (1980). T-S waves due to leading-edge curvature usually have the opportunity to decay significantly

before reaching the streamwise position corresponding to Branch I of the neutral stability curve, since the largest curvature changes occur closer to the nose than the leading-edge-flat-plate juncture. However any instability waves arising from discontinuities at the leading-edge juncture are generally closer to the vicinity of the neutral stability point (beyond which disturbances grow downstream). Therefore, small-scale disturbances near the neutral stability point have the potential to produce large-amplitude instability waves in the boundary layer.

Goldstein's 1985 paper analyzes the effect of a 2-D surface-curvature inhomogeneity as a receptivity mechanism in a Blasius boundary layer. He uses a triple-deck theory composed of three regions: an upper deck describing the inviscid flow outside the boundary layer; a main deck governed to first order by Blasius boundary-layer equations; and a lower viscous deck using unsteady boundary-layer equations in the vicinity of the disturbance. This triple-deck structure provides the appropriate length scales by which long-wavelength disturbances in the inviscid region interact with the small-length-scale curvature inhomogeneity to produce short-wavelength T-S waves.

A complementary view of the mechanism contends that streamwise and normal varying pressure gradients in the freestream forcing amplitude are responsible for the evolution of the unstable T-S waves in the boundary layer (Nishioka & Morkovin, 1986). Additionally, Kerschen (1989) and Kerschen, Choudhari, and Heinrich (1989) have applied triple-deck analysis to several specific examples of 2-D disturbances, including suction strips

and porous surfaces. Receptivity to both acoustic waves and convected gusts has been analyzed.

Receptivity experiments involving 2-D disturbances have been performed by a number of researchers. Aizin and Polyakov (1979) at Novosibirsk investigated receptivity of 12-mm-wide, 12-17- μ m-thin mylar strips to upstream-propagating sound waves using a 60:1 elliptic leading edge. They examined the combination of the Stokes-layer signal and spatially growing T-S signal components. Nishioka and Morkovin (1986) designed experiments at the Illinois Institute of Technology to examine their spatially-varying pressure gradient theory of receptivity. A Blasius boundary layer on a wall was exposed to a weak, harmonic pressure source located normal to the wall. Near field disturbance signal amplitudes and phases were measured downstream along the centerline of the pressure source in order to gain insight into the initial stages of receptivity.

Blasius boundary-layer receptivity due to 2-D roughness strips located at the neutral stability point was examined in a series of tests at Arizona State University. (See Hoos, 1990; Saric, Hoos & Kohama, 1990; and Saric, Hoos & Radeztsky, 1991.) The experiments were conducted using a 67:1 elliptical leading edge, downstream travelling planar sound waves, and 25-mm-wide, 40- μ m-thin roughness strips. Measured T-S wave amplitudes corresponded closely with theoretical predictions. In addition, the stacking of strips produced a linear increase in maximum T-S amplitude until the height of the 2-D roughness element exceeded the height of the lower viscous deck. Also, it was found that the location

of the roughness strip could be finely adjusted in the streamwise direction to “tune” and “detune” the T-S response.

Another series of experiments, sponsored by McDonnell Douglas at NASA Ames, investigated receptivity due to open suction slots and porous suction slots. (See Wlezien, 1989, and Wlezien, Parekh, & Island, 1990.) Sound was injected normal to the flat-plate surface, and the 0.1-mm open suction slot and 7-mm porous slot were both located at Branch I on a flat plate with a 6:1 elliptic leading edge. Receptivity due to the slots was observed for both the no-suction and weak-suction cases, however the receptivity from the leading edge was on the same order of magnitude as the receptivity from the slots, due to the low-aspect-ratio leading edge and freestream turbulence. A 24:1 elliptic leading edge was later machined to investigate a 19-mm perforated strip in the surface of the flat plate. Leading-edge receptivity levels were reduced and receptivity to the perforated strip was demonstrated. In addition, the experiments present a series of techniques for separating the acoustic forcing and T-S response signals in the boundary layer.

Parekh, Pulvin, and Wlezien (1991) investigated receptivity to a spatially periodic freestream disturbance originating from an array of oscillating ribbons and impinging on a 24:1 elliptic leading edge of a flat-plate model. A 0.11-mm forward-facing step was the 2-D receptor in the boundary layer. No T-S waves were identified as originating from the leading edge or the step. Future experimental plans include changing the incidence angle of the gust in order to maximize receptivity as predicted by linear theory.

Two-dimensional roughness strips were used by Kosorygin and Polyakov (1990) at Novosibirsk to destructively interfere with T-S waves due to leading-edge curvature. A semi-circular leading edge provided significant T-S receptivity to acoustic forcing, and by carefully positioning a thin 2-D roughness strip near the neutral stability point, destructive interference reduced the total T-S amplitude below that of the leading-edge-induced T-S level. This experiment was repeated at Arizona State University using a 40- μm -thin 2-D roughness strip to demonstrate both destructive and constructive interference of the roughness-induced and leading-edge-induced T-S wave amplitudes. (Radeztsky, Kosorygin & Saric, 1991)

1.2.4. Receptivity to 3-D Disturbances

Choudhari and Kerschen (1990) examined the theoretical case of acoustic receptivity to 3-D inhomogeneities including a suction region, change in wall admittance, and the presence of a wall “hump”. An asymptotic, high-Reynolds-number, triple-deck analysis was used to predict the downstream disturbance field. It was found to depend on nondimensional forcing frequency, incidence angle of the acoustic forcing, and geometry of the surface inhomogeneity. For certain ranges of nondimensional forcing frequency, they determined that the most unstable waves were oblique and caused the maximum disturbance amplitudes to deviate from the purely downstream direction. Computations for the case of a 3-D roughness element subject to acoustic forcing have been performed by Tadjfar (1990). His results confirm this maximum disturbance amplitude shift from the down-

stream direction in the far disturbance field. (For more details on these, see Sections 2.1. and 2.2.)

An interesting variation on the traditional technique of exciting a single frequency in the boundary layer is found in the experiment by Gaster and Grant (1975). 3-D acoustic pulses were injected into the boundary layer from a small orifice in a flat plate, and measurements were made of the streamwise and spanwise variation of the resulting wave packet. Due to the impulsive nature of the disturbance, a wide band of T-S frequencies is excited. It was found that the wave packets displayed a maximum fluctuation velocity on the centerline of the packet for a significant streamwise distance. However, far downstream, the packets distorted such that the maximum streamwise fluctuation velocities were found off the centerline. Gaster and Grant examined power spectra and determined that these off-centerline maxima were due to the large growth rates of oblique waves which developed downstream of the pulse origin. They attributed the wave packet distortion to nonlinear effects from these rapidly growing oblique waves but also recommended further measurements in an environment with lower turbulence. The results from this experiment are consistent with the recent predictions of obliquely travelling 3-D T-S waves arising from a 3-D disturbance in the boundary layer.

Russian experimenters have also examined 3-D acoustic sources in a Blasius boundary layer. Gilev and Kozlov (1980) investigated 3-D wave packets from a pulsed acoustic source, much like Gaster and Grant. They found that T-S amplitudes on the centerline of the acoustic source decreased far downstream of the pulse origin, as is expected if more

unstable, obliquely-growing 3-D T-S waves are developing. In addition, they compared 2-D and 3-D T-S waves on the centerline of acoustic sources and found that the 3-D maximum T-S amplitude occurs farther from the flat-plate surface and that the second u' maximum in 3-D T-S waves is smaller than that for 2-D T-S waves.

Gilev, Kachanov, and Kozlov (1981) and Kachanov (1984) investigated harmonic acoustic waves injected through a small hole in a flat-plate model. Contours of constant disturbance signal amplitude and phase in the x - z plane are presented and display the heart-shaped disturbance field predicted by 3-D theory. Also, Fourier analysis was used to identify the obliquely travelling waves responsible for the disturbance field shape. At higher forcing frequencies, they determined that the 3-D disturbance field loses its lobed appearance and becomes 2-D in nature.

Mack and Kendall (1983) and Mack (1984) compared results from their experiments using a harmonic acoustic source in a Blasius boundary layer to numeric integration and an asymptotic analysis applied to the problem. With a correction factor applied to compensate for boundary-layer growth, good agreement was found for centerline amplitude measurements and calculations. However, off-centerline amplitude predictions from both numeric integration and asymptotic analysis are less reliable.

1.3. Experiment Objectives

The purpose of the current experiments is to provide insight into the acoustic receptivity of a Blasius boundary layer due to an applied 3-D roughness element. The experiments

are designed to allow comparison with both the theoretical analysis of Choudhari and Kerschen (1990) and the numerical modelling by Tadjfar (1990).

The Arizona State University Unsteady Wind Tunnel is a low-speed, low-turbulence facility designed for receptivity experiments. Both the fan motor and test section are mounted on concrete slabs isolated from the rest of the building. The planar sound field created by the downstream-propagating acoustic waves has been investigated and documented (Saric, Hoos & Kohama, 1990). The model is a flat plate with a near-mirror finish and a 67:1 elliptical leading edge to minimize surface roughness and leading-edge curvature receptivity. In addition, the leading-edge juncture has been wet-sanded and polished by hand to reduce juncture-induced receptivity.

The roughness element chosen for study roughly approximates the Gaussian distribution investigated by Choudhari, Kerschen and Tadjfar. Its maximum height is on the order of the lower viscous deck of triple-deck theory. The three-dimensionality of the disturbance field downstream of the element is documented with streamwise fluctuating-velocity measurements. The data collected from these experiments primarily characterize the near-field response of the 3-D roughness element.

A secondary objective of these experiments is to gain experience in separating the extremely small amplitude of the roughness element T-S response from the “background” signal. This background signal can include components due to the acoustic forcing, leading-edge curvature and juncture receptivity, surface roughness receptivity, environmental disturbances, instrumentation sting vibrations, etc. The signal separation is achieved by

directly measuring the background signal and subtracting it (in the complex plane) from the total signal in the roughness disturbance field.

CHAPTER II

THEORY

Most receptivity theory, computations, and experiments to date have focussed on quantifying the effects of 2-D disturbances on the production of 2-D instability waves. For the 3-D roughness elements under consideration here, 3-D instability waves are generated, and a 3-D theory or numerical analysis is required to predict the disturbance flow characteristics. A main objective of this research is to provide experimental evidence in support of the 3-D stability theory developed by Choudhari and Kerschen (1990) and the numerical model by Tadjfar (1990). Specifically, the following sections address the effect of a single 3-D surface roughness element on a Blasius boundary layer under the influence of acoustic freestream forcing.

2.1. Three-Dimensional Stability Theory

Choudhari and Kerschen (1990) predict instability wave characteristics for a variety of 3-D disturbances, including local wall inhomogeneities of suction, admittance, and height. They use an asymptotic, high-Reynolds-number, triple-deck structure to analyze the flow parameters. A saddle-point method is used to examine the instability wave pattern downstream of the 3-D disturbance.

Triple-deck theory may be used to describe the reaction of a flat-plate boundary layer to a small-scale disturbance on the surface. See Figure 2.1. The total flow over the plate may be classified in three regimes. An “upper deck” pertains to the inviscid, irrotational flow outside the boundary layer. The “main deck” is the inviscid, rotational part of the

boundary layer governed by the Blasius boundary-layer equations, and the “lower deck” is the viscous, rotational portion of the boundary layer governed by the unsteady boundary-layer equations. The 3-D disturbance resides in the lower deck. Boundary conditions are matched asymptotically in the large Reynolds number limit at the edges of the decks. The lower deck is scaled by ϵ^{-5} where ϵ is given by:

$$\epsilon = \left(\frac{U_\infty x^*}{\nu} \right)^{-\frac{1}{8}} \quad (1)$$

U_∞ is freestream velocity, ν is kinematic viscosity, and x^* is the chordwise coordinate measured from the virtual leading edge. (Dimensional quantities are referred to with the superscript “*”). The main deck is scaled by ϵ^{-4} , and the upper deck is scaled by ϵ^{-3} .

Choudhari and Kerschen examine a local wall inhomogeneity of height, a 3-D “hump”. The theoretical hump is modelled by a Gaussian roughness distribution,

$$h = H \exp \left(-\frac{4r^2}{D^2} \right) \quad (2)$$

where roughness height h is determined as a function of radius r , maximum height H and diameter D . Additionally, humps of different aspect ratios are investigated. Freestream forcing is chosen to be time harmonic with a wavelength on the order of sound waves. Planar waves, propagating both parallel to the surface and at an oblique angle are examined.

A 3-D roughness element is found to excite 3-D instability waves in a symmetric, wedge-shaped region downstream of the roughness. From a saddle-point analysis of the

instability wave pattern, three distinct wedge shapes are predicted for three ranges of nondimensional frequency, s :

$$s = c^2 \frac{\omega^* x^*}{U_\infty} \quad (3)$$

For low values of s , on the order of 0.44, the fluctuation-velocity growth rate on the roughness centerline is zero. The disturbance field develops a bi-lobed appearance, as shown in Figure 2.2. For mid-frequency ranges, $s \approx 0.88$, the maximum fluctuation-velocity growth occurs up to $\pm 13^\circ$ from the streamwise direction. The streamwise disturbance growth is less than along these 13° rays, but is nonzero. The obliquely-travelling 3-D T-S waves are the most unstable, producing a “heart-shaped” disturbance field, as may also be seen in Figure 2.2. For high frequencies, $s \approx 1.38$, the maximum fluctuation-velocity growth is directly in the downstream direction. There is no lobed appearance of the disturbance field. This is due to the most unstable waves being almost 2-D at this high frequency.

Receptivity levels for each of these three nondimensional frequency ranges are governed by the aspect ratio of the 3-D roughness element and by the angle of incidence of the acoustic forcing waves. For low frequencies s , a roughness element elongated in the streamwise direction provides increased receptivity. Also, receptivity may be increased by nearly normal-propagating acoustic waves. Conversely, at high frequencies s , receptivity is improved with roughness elements elongated in the spanwise direction and streamwise-propagating acoustic waves. For the mid-frequency range targeted in these experiments, a circular roughness element is the best choice. Receptivity is optimized when roughness

element diameter, D , is set to

$$D = \frac{2\lambda_{TS}}{\pi} \quad (4)$$

where λ_{TS} is the T-S wavelength. Acoustic forcing at a slightly oblique angle also improves receptivity for mid-range nondimensional frequencies.

2.2. Three-Dimensional Stability Computations

Numerical work in the field of 3-D instability waves generated by a 3-D wall inhomogeneity, subject to acoustic freestream forcing, is provided by Tadjfar (1990). High Reynolds number, asymptotic, triple-deck theory is used to analyze the flow, and the 3-D roughness element is modelled with a Gaussian distribution as by Choudhari and Kerschen (1990). The steady basic-state flow is governed by the nonlinear triple-deck equations, and the disturbance flow is governed by the unsteady, linearized, 3-D triple-deck equations, both of which are solved numerically.

The governing parameter in Tadjfar's computations is a scaled Strouhal number, S_o :

$$S_o = \lambda^{-\frac{1}{2}} \epsilon^2 S \quad (5)$$

where ϵ is given in equation (1), λ is the slope of the Blasius profile at the surface, and S is Strouhal number:

$$S = \frac{\omega^* x^*}{U_\infty} \quad (6)$$

A critical value of $S_o = 2.29$ is given as the threshold for growing or decaying disturbance amplitudes (this value of S_o is equal to Choudhari and Kerschen's (1990) $s = 0.44$) and corresponds to Branch I of the neutral stability curve. For S_o less than 2.29, disturbances decay, and conversely disturbances corresponding to S_o larger than 2.29 grow downstream.

Tadjfar's numerical model is in some ways similar to Choudhari and Kerschen's asymptotic theory. Both predict a heart-shaped disturbance wedge characteristic, but Tadjfar's computations display such a wedge pattern only several roughness diameters downstream of the 3-D roughness element. This is in agreement with the earlier 3-D wave packet experiment done by Gaster and Grant (1975). In addition, Tadjfar's computations do not display the three wedge characters listed by Choudhari and Kerschen for different frequency ranges. All results presented for streamwise growing disturbances predict the heart-shaped pattern with a nonzero growth rate on the downstream centerline.

Tadjfar's computations also display an interesting near-field feature of the disturbance wedge not predicted by the asymptotic theory of Choudhari and Kerschen. Prior to development of the heart-shaped wedge, maximum fluctuation-velocity amplitudes lie purely in the streamwise direction. In the downstream direction, the fluctuation-velocity amplitude increases for several roughness radii and then begins to decrease just prior to its deviation from a purely streamwise direction (the development of the symmetric wedge lobes). This phenomenon is shown in Figure 6.19, a mapping of the streamwise disturbance velocity amplitude in the x - z plane. (x and z are scaled by the roughness radius, $D/2$.)

2.3. Experimental Deviations from Theory

A primary focus of this research is to map the disturbance field downstream of a 3-D roughness element and to capture the heart-shaped wedge characteristic predicted by Choudhari and Kerschen (1990) and Tadjfar (1990). The experiment is designed to fall into the medium frequency range outlined by Choudhari and Kerschen. However, experimental work by nature is difficult to exactly mold into a particular theoretical or computational case. Inevitably differences will exist between the purely mathematical world and the tests.

The major source of difference in this experiment is the 3-D roughness shape. Gaussian “humps” with a maximum height much less than a millimeter are difficult to design from laboratory materials. The Gaussian roughness distribution in these experiments was modelled by stacked circular roughness elements. Six layers of a 3-M low-tack-adhesive tape were piled for a total roughness height of $240\ \mu\text{m}$. Two each of three different diameters were used, as shown in Figure 2.3. A comparison of this design with a true Gaussian distribution is given in Figure 2.4. The expected result of this discrepancy is excitation of a finite number of 3-D T-S modes rather than an infinity of modes.

CHAPTER III

EXPERIMENTAL FACILITY AND EQUIPMENT

To perform sensitive receptivity experiments, it is necessary to work in a carefully controlled environment and to use high-quality signal conditioning equipment. A guide to basic requirements in receptivity experiments is provided by Saric (1990). Drawings of the ASU Unsteady Wind Tunnel are shown in Figure 3.1. For a detailed description of the wind tunnel, flat-plate model, and 3-D traversing system, see Appendix A.

3.1. Sound System

Sound waves are introduced in the plenum upstream of seven screens and aluminum honeycomb. See Figure 3.2. To avoid blockage and flow disruption, the rectangular box containing the speaker is mounted outside the tunnel. The speaker face protrudes through a hole in the tunnel wall such that it is flush with the inside of the tunnel. In this manner, downstream-travelling sound waves are planar in the y - and z -directions, and are normal to the flat-plate leading edge.

The speaker is an 8-ohm Fosgate 254-mm woofer. An Adcom twin stereo amplifier drives the speaker, and input to the amplifier is provided by a Model SD1041-5 Sweep Oscillator. The speaker is rated at 225 watts, but when operated at a single frequency the power output is limited to 100 watts, producing a freestream acoustic disturbance of approximately $|u'| = 0.015$, or 95 dB.

3.2. Roughness Specifications

A 3-M low-tack-adhesive polyester tape was chosen for the applied roughness elements. The tape adheres securely to the aluminum surface, yet is easy to remove without marring the flat-plate model. No residue is left behind after removing the tape. The tape has a uniform thickness, including the adhesive backing, of 40 μm and a width of 25.4 mm. In addition, it is the material used in standard 2-D roughness experiments at the ASU Unsteady Wind Tunnel (Hoos, 1990).

A disadvantage of choosing tape for the roughness elements is that the elements can not be reused. The layers are cut by hand with a razor blade to ensure that edges remain completely smooth. After application, the element is pressed firmly to the surface, and during removal layer edges become rough. Therefore, some uniformity in layer diameters is sacrificed to maintain uniform roughness thickness. This was deemed a necessity after detecting vorticity caused by roughened tape edges resulting from a tool used for cutting and reapplication of the elements.

3.3. Freestream Control

Freestream tunnel conditions are continuously monitored by an in-house-written code running on a dedicated personal computer. The computer samples temperature, static and dynamic pressures and calculates test section speed and chord Reynolds number. The code has been nicknamed “cruise control” for the tunnel because it also is used to control tunnel fan speed. The user specifies a particular dynamic pressure, speed, or chord Reynolds number and the code uses a feedback loop to maintain a constant operating condition. An

option to hold fan speed constant is used for these experiments to avoid any unsteady flow characteristics.

Test section temperature is measured by a thermistor built and calibrated by Dr. Shohei Takagi. Static and dynamic pressures are measured by a pitot probe connected to two MKS type 390HA-0100SP05 temperature-compensated transducers, 1000 and 10 torr, respectively. The pressure signals are monitored by two 14-bit, MKS Type 270B Signal Conditioners.

3.4. Signal Analysis Equipment

Mean flow and fluctuation velocities are measured in the freestream and boundary layer using two hot-wire probes. Five-micron tungsten wire is used on both hot-wires. DISA hot-wire anemometry equipment includes two each of a Main Unit #55M01, Power Pack #55M05, and Constant-Temperature Anemometer (CTA) Bridge #55M10. CTA bridge output signals are monitored by two Fluke 8050A Digital Multimeters and acquired directly for boundary-layer and freestream mean flow measurements.

The fluctuation components of the CTA bridge output signals are removed from the DC signal, filtered, and amplified by a Stewart VBF44 Dual Two Channel Filter. The Stewart filters have excellent attenuation characteristics, with a slope of 135 dB per octave. In addition, active filter control is implemented through an RS-232 interface with the Concurrent (Masscomp) 5600 Data-Acquisition system. The fluctuation signals are then monitored using a Tektronix Eight Channel Oscilloscope, Models #5440, #5A14N, and

#5B42. Again, before being acquired, the signals are monitored by two Fluke 8050A Digital Multimeters.

CTA Bridge output signal phase and magnitude is measured by a Stanford Lock-In Amplifier, Model #SR530. The tracking signal for the lock-in amplifier is provided by a Model SD1041-5 Sweep Oscillator, the same device providing the speaker driving frequency. The lock-in amplifier output of ± 9 V for both signal magnitude and phase is reduced to ± 4.5 V by two resistor boxes, each containing two 50 k Ω resistors. This is necessary to make the output compatible with the ± 5 V limitation on the acquisition A/D board.

All signals are connected to an eight channel in-house-built differential box. The signals from the differential box are acquired by a 12-bit, 16 channel, 1 MHz, A/D board in the primary data-acquisition computer, a Concurrent (Masscomp) 5600. All data are acquired and analyzed in real time. Real-time data plots are displayed on a 19 inch, color, 1152 \times 910 pixel monitor. For intensive data analysis and additional data storage two DECstation 5000/200 computers are also used. These are equipped with magnetic tape drives so that all data storage, and daily system backups are accomplished in-house. All ASU Unsteady Wind Tunnel computers are networked via Ethernet on a sub-net with one another and to the remainder of the university network. A Digital dot-matrix printer, Hewlett Packard 7475A pen plotter, and Apple Laserwriter are used for hard copies.

CHAPTER IV

EXPERIMENTAL TECHNIQUES

Experimental parameters are chosen such that these tests correspond as closely as possible to the cases outlined by Choudhari and Kerschen (1990) and Tadjfar (1990). The extremely low-level disturbance-signal amplitudes which were encountered necessitated the use of new techniques to decisively separate the effect of the 3-D roughness element from the background signal. In addition, a scheme is developed to map the three-dimensionality of the disturbance field downstream of the roughness element.

4.1. Scaling the Experiment

As detailed in Section 2.1., Choudhari and Kerschen (1990) predict that the characteristics of the disturbance field just downstream of a 3-D inhomogeneity depend on the value of a nondimensional forcing frequency, s . These experiments are scaled to produce a roughly heart-shaped disturbance field resulting from mid-range values of s , on the order of 0.88. Maximum disturbance-signal amplitudes are expected to lie off the centerline of the roughness element by an angle of approximately $\pm 13^\circ$.

The 3-D roughness element is composed of six circular layers of 40- μm -thin polyester tape. It is designed to approximate the Gaussian roughness distribution examined by Choudhari and Kerschen (1990) and Tadjfar (1990). (See Figures 2.3 and 2.4.) The 3-D roughness element used in these experiments is not expected to excite an infinity of 3-D T-S modes as a Gaussian roughness distribution would. Since it is composed of three different diameters of circular elements, it will excite only a finite number of T-S modes. This

approximation is made due to the difficulties associated with constructing a 3-D roughness element with total height of $240\ \mu\text{m}$ and a Gaussian roughness distribution.

A maximum roughness diameter of 25 mm is chosen based on restrictions of the roughness material. For optimum excitation of the 3-D T-S waves, this sets λ_{TS} at $\pi D/2$, or 40 mm. Next, choosing a freestream velocity of 15 m/s, the following parameters are specified by Branch I of the neutral stability curve: $F = 55 \times 10^{-6}$; $R = 582$; $k_r = 0.01$; and $x^* = 383$ mm. This x^* corresponds to a position 110 mm downstream of the leading-edge juncture. The F translates to a dimensional frequency $f = 116$ Hz. This is sufficiently far from the instrumentation sting natural frequency of 75.8 Hz but suspiciously close to the electrical line frequency, 120 Hz.

Operating the speaker this close to the line noise harmonic would not be possible without exceptional filters. As described in Section 3.4., the Stewart filters have excellent attenuation characteristics, with a slope of 135 dB per octave. In the freestream disturbance signal, the line noise amplitude is 20 dB higher than the background signal noise. The disturbance sound amplitude is 15 dB higher than the line noise. In the boundary-layer disturbance signal, the line noise exceeds the background by 10 dB and the sound amplitude is 20 dB higher than the line noise. See Figures 4.1 and 4.2. These ratios are sufficiently large to assure no line-noise contamination of the hot-wire signals.

Speaker sound pressure level is chosen in order to maximize disturbance-signal amplitudes. The speaker is driven at two voltages, 24 V and 28 V. These correspond to a freestream $|u'|$ of 1.5×10^{-4} and 1.7×10^{-4} , respectively. Sound pressure level is

calculated according to the following formulas:

$$p' = \rho c |u'| \quad (7)$$

$$SPL = 20 \log_{10} \left(\frac{p'}{20 [\mu\text{Pa}]} \right) \quad (8)$$

The speaker is operated at 93 and 95 dB to provide freestream disturbances.

The parameters outlined above yield a nondimensional frequency $s = 0.78$, where s is given by (3). This is close to the mid-range $s \approx 0.88$ suggested by Choudhari and Kerschen (1990). Due to the small signal amplitudes encountered under these conditions, the roughness was also moved $12D$ downstream of Branch I to a second location, $x^* = 688$ mm. Changing only this parameter, the nondimensional frequency corresponding to the second roughness position is $s = 1.20$. This falls between the mid- and high-frequency ranges, with the latter at $s \approx 1.38$. Note that all data are taken with $U_\infty = 15$ m/s and $F = 55 \times 10^{-6}$.

In order to keep the roughness element on the order of the lower viscous deck, the roughness altitude is limited to $240 \mu\text{m}$. The lower viscous deck scaling variable, Y , is given by:

$$Y = \frac{y^*}{\epsilon^5 x^*} \quad (9)$$

where y^* is the normal to the surface coordinate, x^* is the chordwise coordinate measured from the virtual leading edge, and the small scaling parameter ϵ is given by (1). $Y_r = 1.8$ for the position $x^* = 383$ mm and $Y_r = 1.4$ for the $x^* = 688$ mm case.

4.2. Roughness Signal Discrimination

Note that although the 3-D roughness element is placed at Branch I, measurements are not taken at Branch II, where disturbance signals are most amplified. Instead, the disturbance field immediately downstream of the roughness element is investigated. It is characterized by extremely small amplitudes, with a maximum on the order of $u' = 4 \times 10^{-4}$. The background signal level is also near this level, around 2×10^{-4} , and in general the effect of the roughness element is not convincingly visible above the background signal level.

This difficulty was also encountered by Wlezien, Parekh, and Island (1990) in their experiments. They propose that this background signal is a Stokes wave produced by the acoustic forcing of the boundary layer. Using the fact that the Stokes layer has a wavelength on the order of the sound waves, several methods are suggested to separate the long-wavelength Stokes component from the short-wavelength T-S component of the signal.

One proposed method involves operating at an extremely low velocity, as low as it is still possible to obtain an accurate hot-wire velocity calibration. In this manner, the Stokes layer should dominate the T-S signal, and its magnitude may be measured directly. In Figure 4.3, the data from a boundary-layer disturbance profile at $U_\infty = 5$ m/s are plotted with the theoretical Stokes layer at these conditions. It is clear that even at this low velocity other factors are contributing to the disturbance profile.

A second technique suggested by Wlezien, et. al., involves using polar plots to separate the long-wavelength acoustic signal component from the short-wavelength T-S component. Disturbance amplitudes and phases are measured at a series of points constant in the y and z directions, but closely spaced over approximately a T-S wavelength in x . In this short streamwise distance, the phase and magnitude of the long-wavelength acoustic component vary only slightly, by $\theta_{ac} = 5^\circ$ and $\lambda_{TS}/\lambda_{ac} = 0.013$, while the T-S phase makes a 360° circuit and its amplitude visibly increases. An algorithm is devised to determine the “center” of the T-S wave “circle” from the polar plot. This center point defines the magnitude and phase of the acoustic wave at a specific streamwise location and boundary-layer position. Subtracting it in the complex plane from the total disturbance signal should produce the T-S wave amplitude and phase. In order to map the acoustic signal and the T-S wave throughout the boundary-layer thickness, it is necessary to repeat this technique over a series of altitudes within the boundary layer. By applying the technique to a series of boundary-layer disturbance profiles spaced over a T-S wavelength in the streamwise direction, the Stokes layer and T-S wave over a streamwise increment may be measured. Applying the technique to this experiment produced disappointing results. There is tremendous scatter in the data, and a T-S wave is only vaguely decipherable from the boundary-layer profiles.

Several factors are responsible for the failure of this intriguing technique in these experiments. The first is large scatter, arising from extremely small signals. More fundamentally, the “total” signal measured has more components than just a roughness-element

induced T-S wave and an acoustic wave. It is known that the instrumentation sting is not perfectly vibration-free. At these signal magnitudes, any vibration component has the potential to be a serious problem. Also, as evident from the attempt to directly measure the Stokes layer at a low velocity, "background" T-S waves are present. These are potentially caused by the leading-edge contour and juncture, and by surface roughness. For these reasons, the roughness discrimination techniques proposed by Wlezien, et. al., were not sufficient for these experiments.

An important difference between the experiments of Wlezien, et. al., and these is removability of the 3-D inhomogeneity. The types of inhomogeneities used by Wlezien are not as easily removed as the low-tack-adhesive tape chosen for this experiment. Therefore, without specifically determining the components of the background signal, in this experiment it is possible to measure its amplitude and phase directly by taking data with the roughness element removed. In this manner, the conglomerate background signal may be subtracted from the total signal in the complex plane yielding only the effect of the 3-D roughness element at every data point. See Figure 4.4. This technique eliminates the Stokes layer, T-S waves from the leading edge, T-S waves from surface roughness, and instrumentation sting vibrations.

Although scatter is not eliminated, the technique succeeds in convincingly discriminating the portion of the signal due to the applied 3-D roughness element from the total disturbance signal. See Figure 4.5 for a verification of the technique using a 2-D roughness strip placed at Branch I; data are taken at Branch II. The data are plotted with the

theoretical, 2-D T-S wave amplitude and phase. Figure 4.6 shows a sample run with the 3-D roughness element. The “*” data are u' magnitudes and phases with and without the roughness element on the surface, while the “+” points are the subtracted signal, or the effect of the 3-D roughness element only.

4.3. Three-Dimensional Disturbance Mapping

In order to investigate the roughness disturbance field in three dimensions, two types of testing runs are used. The first is a spanwise traverse, beginning 30 mm in z^+ above the roughness centerline and ending 30 mm below it. These scans are taken at a constant height in the boundary layer and at a constant streamwise position. Data are taken every 1.5 mm for a total of 41 points over the full 60 mm. Seven of these spanwise scans, or “z-scans”, are taken with the roughness at Branch I. The first five are taken at half-roughness-width intervals, beginning one roughness width, D , downstream of the element’s center. The remaining two z-scans are taken $6D$ and $12D$ downstream of the roughness center. See Figure 4.7 for Branch I testing locations.

The second type of measurement scheme used is a boundary-layer disturbance profile. Profiles map the depth of the boundary layer at a particular spanwise and chordwise position. The profile begins slightly outside the boundary layer and steps into the boundary layer with progressively smaller steps, specified by:

$$(\text{next step}) = (\text{last step}) \times U \quad (10)$$

A typical initial step is 0.2 mm and a final step is $25\text{ }\mu\text{m}$ at $U = 0.07$. Profiles typically include 40 points. At the Branch I roughness position, a series of six profiles are taken at a streamwise location $2.5D$ downstream of the element's center. This series of profiles begins on the roughness centerline and extends 30 mm in the negative z direction, with each profile 6 mm apart. (See Figure 4.7.)

All measurements with the roughness element in the Branch I position are taken at a $SPL = 93\text{ dB}$. In an attempt to increase signal magnitudes, data are also taken with the roughness $12D$ downstream of Branch I. At this location, all measurements are taken at both the 93 and 95 dB sound pressure levels. Sixty-millimeter z -scans are taken $1.5D$, $2.5D$, and $3.5D$ downstream of the element's center. Six profiles are again taken at 6 mm intervals on the $2.5D$ -downstream z -scan. Figure 4.8 shows downstream testing locations.

CHAPTER V

DATA ACQUISITION

Standard codes in use at the ASU Unsteady Wind Tunnel were used intact or modified for this project. All codes were written in C. Of interest is the use of temperature compensation on all voltages output by the hot-wire anemometers. Also, a Stanford Lock-In Amplifier was used for relative phase measurements and as a second amplitude measuring device for the boundary-layer disturbance signal.

5.1. Preparation and Calibration

Before a series of tests, a number of preliminary tasks must be completed. First, the hot-wire anemometer bridges must be balanced. Next, a square wave is input to the anemometers, and response characteristics are optimized by adjusting capacitance and inductance. An optimum response has as little overshoot and oscillation as possible.

During warm-up of the wind tunnel, hot-wire voltage change with temperature is monitored for both wires. The slopes of the resulting lines, the "temperature coefficients," are used for the hot-wire calibration and in all data acquisition codes. These coefficients remain accurate for a temperature increase in excess of 10 C. Hot-wires are calibrated over the range of velocities expected for the experiment, in this case from 1 to 18 m/s. The temperature at the first point is taken as the calibration temperature and all subsequent calibration point voltages are adjusted using the temperature coefficients. In this manner, a nearly constant tunnel temperature is not required for hot-wire calibration. A least-squares fitting routine is used to fit a fourth-order polynomial to the calibration curve.

5.2. Sample Data

For each data point taken in a spanwise traverse, the following quantities are measured: temperature; boundary-layer relative phase; boundary-layer and freestream mean flow; and, boundary-layer and freestream normalized streamwise fluctuations. In a boundary-layer disturbance-profile run, boundary-layer streamwise fluctuation is filtered and amplified by both the Stanford Lock-In Amplifier and the Stewart Filter unit. This redundancy provides a check for both pieces of equipment.

Temperature is measured by a thermistor. The DC voltage output is acquired at the same time as the hot-wire anemometer DC voltage components. These three signals are acquired differentially by the Masscomp's A/D board at a frequency of 500 Hz for 15 sec. Nearly simultaneous sampling of the channels is provided by setting the Masscomp's burst frequency to 500,000 Hz. The temperature voltage reading is converted to degrees C by a calibration equation.

The AC components of the hot-wire anemometer outputs are sent to a Stewart Dual Two Channel Filter for filtering and amplification. A two-hertz filtering window is created by low-passing at 117 Hz and high-passing at 115 Hz. The Stewart unit may be remotely controlled and the boundary-layer disturbance-profile code uses a routine to adjust the signal amplification appropriately throughout the boundary layer. This is necessary due to large changes in boundary-layer AC signal amplitude in these runs. Typical amplification ranges from 50 to 70 dB. The conditioned signals are acquired at 1000 Hz for 20 sec.

Once acquired, the DC hot-wire signal components are converted to mean-flow velocities using the calibration curves. AC rms voltages are added and subtracted from the appropriate DC voltages and passed through the calibration curves to obtain velocity fluctuations about the mean-flow velocity for both channels. Finally, before recorded, the fluctuation velocities are normalized by U_{∞} .

Boundary-layer phase relative to the freestream ac signal phase is measured by the Stanford Lock-In Amplifier. At the beginning of the run, the freestream anemometer output is sent to the Stanford input. The Stanford unit is operated in the "R/ ϕ " mode. Depressing the relative ϕ button forces future output to read relative to the current input. The freestream signal is removed and the boundary-layer signal connected for the run. The Stanford Amplifier outputs DC voltages corresponding to AC signal magnitude and phase. The raw outputs are ± 10 V. Since the Masscomp A/D board supports only ± 5 V or 0 to 10 V, a voltage reducing device was built to halve the maximum Stanford output. These signals are acquired at 500 Hz for 15 sec. The boundary-layer fluctuation velocity measured in this way serves as a check against the Stewart filters.

5.3. Codes

The following is a list and short description of all codes used in this experiment.

TCOMP: During wind tunnel warm-up, this routine measures the change in both hot-wire channel voltages with change in temperature. The output, a temperature coefficient for each channel, is used in the hot-wire calibration program and in all software which acquires hot-wire DC voltages.

CALHW2: This temperature-compensated program calibrates both hot-wire channels using dynamic pressure measured by a pitot probe. The calibration temperature is the temperature at the first point of calibration. Successive raw voltages are temperature compensated before being recorded.

BL: There are two versions of this program, BL.REG and BL.STEP. BL.REG measures mean flow and fluctuation velocity profiles. BL.STEP is the version which reads its y step sizes from an input file rather than calculating step size from the current U . BL.REG is used for a profile with the roughness element, and the without-roughness profile is taken with BL.STEP. At each data point, a boundary-layer relative phase and signal magnitude are measured by the Stanford Lock-In Amplifier. BL records y step values, but not absolute y position. This is computed by BLAS.

BLAS: Given the BL output file and the run temperature and pressure, BLAS extrapolates the absolute position of the plate surface using the Blasius boundary-layer profile. A straight line is fit through a user-specified set of points close to the surface. BLAS output includes the surface position, Blasius profile slope near the the surface, virtual leading edge, displacement thickness, δ^* , momentum thickness, θ , and shape factor, H .

TSPROFILE3: A series of with-roughness and without-roughness boundary-layer disturbance profiles measured by BL are subtracted in the complex plane. The output is a series of T-S profiles due to the effect of the applied roughness only.

SCANZ: Data are acquired over a spanwise traverse of the boundary-layer at user-specified increments. Constant user-specified U is maintained within ± 0.005 by adjusting

hot-wire position in y . Boundary-layer disturbance phase is recorded in addition to mean-flow and fluctuation velocities. Actual position in y is calculated from BLAS output parameters and recorded.

TSSCANZ: Data from a series of with-roughness and without-roughness spanwise boundary-layer traverses taken by SCANZ are subtracted in the complex plane. The output is a series of T-S amplitudes and phases over the spanwise traverses.

Note: The following are codes used in the development of the final roughness-signal discrimination technique. These were not used for the results presented in Chapter VI.

SCANX: Data are acquired over a streamwise traverse of the boundary-layer at user-specified increments. Constant user-specified U is maintained by adjusting hot-wire position in y according to the Blasius boundary layer. Boundary-layer disturbance phase is recorded in addition to mean flow and fluctuation velocities. Actual position in y is calculated from BLAS output parameters and recorded.

ACOUDIST: Data from a single SCANX run are analyzed to separate the long- and short-wavelength components. Output is the magnitude and phase of the long-wavelength component.

ACVECT: A series of boundary-layer disturbance profiles are taken with BL.STEP in the streamwise direction. At each y position in the boundary layer, the long- and short-wavelength signal components are separated, as in ACOUDIST. The output is a long-wavelength signal profile.

TSPROFILE2: ACVECT output, a long-wavelength signal profile, is subtracted in the complex plane from each of a series of disturbance boundary-layer profiles.

CHAPTER VI

RESULTS

An important aspect of this research has been the ability to overcome the problems associated with measuring exceptionally small signal amplitudes. Extreme care was taken with all measurements. Without the signal subtraction technique used, the portion of the streamwise fluctuation-velocity signal due only to the applied 3-D roughness element is barely visible above the background signal. By measuring the magnitude and phase of each position in the boundary layer both with and without the roughness element, it was possible to subtract the signals leaving only the effect of the 3-D inhomogeneity.

However, due to the sensitivity of the experiments, many factors may still affect the measurements. Any misalignment in position between the measurement locations of the with and without roughness data points would be a source of error in the subtracted signal. Also, changes in testing conditions over the time frame between the measurement of the two signals could affect the resulting signal. Every effort was made to minimize error from these sources. However, simply due to the errors associated with subtracting small signals, there is considerable scatter apparent in the data. The results should be viewed in a more qualitative than quantitative sense.

6.1. 3-D Roughness at Branch I

Initially the 3-D roughness element is placed at Branch I of the neutral stability curve. All measurements with the roughness element in this position are taken at $U_\infty = 15$ m/s, $F = 55 \times 10^{-6}$, and a freestream disturbance $SPL = 93$ dB.

6.1.1. Spanwise and Streamwise Variation of u'

Figures 6.1 through 6.4 map the streamwise velocity-fluctuation amplitude and relative phase in the x - z plane at a constant $U(y)$. This value is chosen to be near the position of maximum disturbance signal amplitude in the y direction. Figures 6.1 and 6.2 show a series of five runs, with each run corresponding to a different streamwise position, x . (x and z are measured from the roughness center and scaled by D .) The series shows $D/2$ increases in streamwise position ranging from D to $3D$ downstream of the roughness element. Figures 6.3 and 6.4 give a series of three runs at streamwise locations of $3D$, $6D$, and $12D$. The span of the runs extends over $2D$ in the z direction.

Figures 6.2 and 6.4 give relative phase values for the data. The apparent jumps in the plots often correspond to phase "wrap-around" from $-\pi$ to $+\pi$. More interesting information is obtained from the disturbance-velocity amplitudes given in Figures 6.1 and 6.3.

In Figure 6.1, particularly on the run D downstream of the roughness center, some points in the $-z$ -direction have unexplainably high amplitudes. Neglecting these, there is no measurable effect of the 3-D roughness element this close to it. Beginning at the $3D/2$ run and extending downstream, the effect of the roughness element may be seen. There is growth of the signal amplitude, but it is difficult to determine the angle at which the disturbance field expands in the spanwise direction. In the streamwise direction, there appears to be an increase of the disturbance amplitudes, followed by a slight decay at the

$5D/2$ location, and subsequent continued growth. This characteristic is predicted in the near-disturbance-field computations by Tadjfar (1990) and will be discussed in Section 6.3.

Note that Figures 6.3 and 6.4 are an extension in the streamwise direction of Figures 6.1 and 6.2. The $3D$ run from the previous figures is included, as well as runs at $6D$ and $12D$. By $6D$ downstream of the roughness center, it is expected that the predicted heart-shaped disturbance-wedge characteristic would be apparent in the signal amplitudes. From this run, there is no evidence of the predicted behavior. Farther downstream at $12D$, the run does not extend far enough in the spanwise direction to detect any lobed characteristics. However, there also does not appear to be significant u' growth on the roughness element centerline, as would be expected if there was no heart-shaped disturbance field development.

6.1.2. Spanwise and Normal Variation of u'

Figures 6.5 through 6.8 display spanwise variation of the boundary-layer disturbance profiles. Again, Figures 6.5 and 6.7 give u' amplitudes and Figures 6.6 and 6.8 give relative signal phases. The runs shown in these figures are taken at a streamwise position $2.5D$ from the roughness center. Note that in some of the runs there are irregular data points near the surface of the flat plate. This is most likely due to very slight misalignments in the with and without roughness data-point positions. The distance between the individual data points becomes increasingly small during the run as the hot-wire approaches the flat-plate surface, with final points separated by $25\ \mu\text{m}$. A very small misalignment between runs would cause significant error in this region. In addition, this is the region in which the smallest signals are being subtracted, which could also contribute to error.

Figures 6.5 and 6.6 include five runs, ranging from spanwise locations of $-D$ to $+D$ by $D/2$. At this streamwise position, the range of the influence of the 3-D roughness element does not appear to extend beyond D on either side of the centerline of the element. The run taken on the roughness centerline has a characteristic 3-D T-S disturbance profile. Figures 6.7 and 6.8 include a series of six disturbance profiles, ranging from 0 to $-2.5D$ in the spanwise direction. The data in this set becomes less reliable as distance in the spanwise direction increases. It is included more for completeness than argument.

6.2. 3-D Roughness Downstream of Branch I

Due to the exceptionally small signal amplitudes encountered during these experiments and the significant scatter in the data, two changes were made to increase signal amplitudes. The first was moving the roughness element $12D$ downstream of Branch I (but still well upstream of Branch II) and the second was increasing freestream forcing levels. Each set of runs presented in this section was taken with U_∞ and F unchanged, and with freestream forcing at two levels, $SPL_1 = 93$ dB and $SPL_2 = 95$ dB. To avoid nonlinear freestream forcing, larger acoustic sound pressure levels were not used. These two modifications to the experiment parameters did increase signal amplitudes, but only slightly.

6.2.1. Spanwise and Streamwise Variation of u'

Figures 6.9 through 6.12 display streamwise and spanwise variation of disturbance-velocity amplitude and relative phase at a constant $U(y)$, chosen to correspond to a y -position near maximum u' . Freestream forcing in Figures 6.9 and 6.10 is 93 dB, while the

sound-pressure-level in Figures 6.11 and 6.12 is 95 dB. Runs are taken at the $1.5D$, $2.5D$, and $3.5D$ streamwise stations and extend approximately $2D$ in the spanwise direction. Both amplitude and relative phase measurements are presented.

Figures 6.9 and 6.11 are qualitatively similar. The $1.5D$ station run displays only a very slight effect of the roughness element. Signal amplitudes have grown significantly by $2.5D$ downstream of the roughness element, and there is a slight decrease in signal amplitude in the $3.5D$ run. This is the characteristic of the near-field fluctuation-velocity amplitude predicted by Tadjfar's (1990) numerical modelling. (See Section 6.3.) The data are still not clear enough to determine the angle of spanwise spreading of the disturbance field.

6.2.2. Spanwise and Normal Variation of u'

Figures 6.13 through 6.16 display two sets of six boundary-layer disturbance profiles taken with freestream SPL of 93 dB and 95 dB. Each series of profiles extends over a range of spanwise locations from the roughness centerline to $-2.5D$ in the z -direction. All data in these figures are taken at a constant streamwise position located $2.5D$ downstream of the roughness center. Figures 6.13 and 6.15 are fluctuation velocities, and Figures 6.14 and 6.16 are relative phase measurements.

With the exception of a few data points close to the surface of the flat plate, the disturbance-velocity profiles taken at the zero spanwise location closely resemble 3-D T-S waves. This discrepancy at the surface is most likely due to very small misalignments in position, which can produce large errors in this region. The fluctuation-velocity amplitudes

decrease in the spanwise direction until there is essentially no effect of the roughness at the $-2.5D$ spanwise location. While these general trends hold for both Figures 6.13 and 6.15, the shapes of the individual profiles, particularly in the $-0.5D$ to $-2D$ region, do not match between the two series of runs. It is difficult to determine what is happening in this region, again due to small signal amplitudes and scatter in the data.

6.3. Comparison with Numerical Model

It is interesting to qualitatively compare the results of these experiments and data from the numerical model by Tadjfar (1990). Tadjfar presents contour maps of fluctuation-velocity amplitudes for nondimensional frequency S_o of 2.0 and 3.0. Using (5) in Section 2.2. to calculate S_o for the two roughness positions tested yields values of $S_{o,1} = 4.1$ and $S_{o,2} = 6.3$. However, Tadjfar's computations are based on the high-Reynolds-number limit, and these values must be adjusted to compensate for finite Reynolds numbers. For the case of the roughness element at Branch I, the procedure is relatively straightforward, giving an effective nondimensional frequency $F_{eff,1} = 25 \times 10^{-6}$. Translating to Tadjfar's nondimensional frequency, $S_{o,eff,1} = 1.9$, which is close to the 2.0 case presented. For the experimental case of the 3-D roughness downstream of Branch I, the procedure necessary to compensate for finite Reynolds number is less straightforward. Noting the effect of compensation on the Branch I case, assuming a $S_{o,eff,2}$ of 3.0 for comparison is a reasonable first-order estimate.

Tadjfar's results presented here are for a roughness height of $Y_r = 1.0$, where Y is the lower-viscous-deck scaling variable given by (9) in Section 4.1. With the 3-D roughness

element at Branch I, the height of the element is $Y_{r,1} = 1.8$ and in the downstream position the height is $Y_{r,2} = 1.4$. Again, these values are close enough to provide a qualitative comparison between the numerical and experimental results.

For the 3-D roughness element at Branch I, Figures 6.1 and 6.3 map the disturbance velocity amplitude in the x - z plane. The corresponding numerical mapping is given in Figure 6.17. (Note that the x and z axes are scaled by $D/2$.) There is little agreement between the two. Maximum disturbance amplitudes are predicted to occur at a streamwise position D downstream of the roughness center, whereas in the experiments this station corresponded to the smallest disturbance amplitudes measured. By the $6D$ downstream position, the disturbance field has begun developing the heart-shaped characteristic in the computations. There is no evidence of this behavior in the experiments. The only similarity found between the two is the centerline increase and subsequent decrease of fluctuation-velocity amplitude, albeit on drastically different length-scales.

Computational mapping of the x - y plane at $z = 0$ for the roughness element at Branch I is given in Figure 6.18. The y axis is scaled by the roughness height, Y_r . The corresponding experimental mapping is the zero-span disturbance-profile from Figures 6.5 and 6.7. From the experimental data, the altitude of maximum disturbance-velocity in the profile is $\eta \approx 1.3$, or $y^* \approx 0.93$ mm. At the $2.5D$ streamwise position in Figure 6.18, the height of maximum u' is $Y \approx 4.0$, or 0.96 mm. Agreement between the computations and experiment is quite good here.

Similar comparisons can be made between the downstream-roughness-position experiments and the $S_o = 3.0$ computations. The streamwise stations 3, 5, and 7 in Figure 6.19 correspond to the $3D/2$, $5D/2$, and $7D/2$ runs in Figures 6.9 and 6.11. Here the experimental trend of initially increasing and then decreasing centerline u' amplitudes is depicted in the numerical results on the correct length-scales. Looking at the x - y plane, Figures 6.13 and 6.15 show a maximum u' at $\eta \approx 1.3$, or $y^* \approx 1.2$ mm, on the roughness centerline. In Figure 6.20, the maximum value is located at $Y \approx 4.2$, or $y^* \approx 1.0$ mm. Again, there is good agreement between the major features of the experimental data and the computational results.

CHAPTER VII

CONCLUSIONS

These experiments examine the disturbance velocity field downstream of a 3-D roughness element in a Blasius boundary-layer under the influence of freestream acoustic waves. Characteristics of this disturbance-field have been predicted by the asymptotic, high-Reynolds-number, triple-deck theory of Choudhari and Kerschen (1990) and by the numerical analysis of Tadjfar (1990). The objective of these experiments is to map the 3-D disturbance field in order to provide experimental data in support of these analyses and to obtain greater insight into the development of 3-D T-S instability waves.

An important aspect of this research has been the ability to discriminate the 3-D, roughness-induced, T-S portion of the fluctuation-velocity signal measured. Experimental u' amplitudes are on the order of 10^{-4} and presumably contain components from leading-edge T-S waves, surface roughness T-S waves, instrumentation sting vibrations, and the Stokes layer, in addition to the desired 3-D roughness-induced T-S signal. In order to discriminate the 3-D roughness-induced T-S amplitude, data are taken both with the roughness element in position and with it removed from the flat-plate model. Signal amplitudes and phases are measured and subtracted in the complex plane, leaving only the 3-D T-S magnitude and phase.

Data are presented to show the streamwise and spanwise variation of u' at a constant $U(y)$ and the spanwise and normal variation of u' at a constant streamwise position. The 3-D roughness element is placed at two streamwise positions, Branch I and 12D

downstream of Branch I. In this manner, the growth of the disturbance-field wedge pattern downstream of the roughness is documented in the streamwise and spanwise directions.

Most measurements focus on the near-field region immediately downstream of the 3-D roughness element. The evolution of the 3-D T-S waves is documented, and it is likely that the disturbance field at these streamwise positions has not fully developed. The “heart-shaped” disturbance-wedge predicted by Choudhari and Kerschen’s 3-D T-S theory is not observed. However, some near-field characteristics of Tadjfar’s numerical model are found, particularly for the case of the roughness element downstream of Branch I. Future investigations into the effect of a 3-D roughness element should extend the measurement regime farther downstream to determine if the heart-shaped disturbance field does eventually develop.

REFERENCES

- AIZIN, L. B. & POLYAKOV, N. F. 1979 Acoustic generation of Tollmien-Schlichting waves over local unevenness of surfaces immersed in streams (in Russian). Preprint 17, Akad. Nauk, USSR, Siberian Div., Inst. Theor. & Applied Mech., Novosibirsk. (see Nishioka & Morkovin, 1986).
- CHOUDHARI, M. & KERSCHEN, E. J. 1990 Instability wave patterns generated by interaction of sound waves with three-dimensional wall suction or roughness. *AIAA Paper No.* 90-0119.
- GASTER, M. & GRANT, I. 1975 An experimental investigation of the formation and development of a wave packet in a laminar boundary layer. *Proc. R. Soc. Lond. A* **347**, 253-269.
- GILEV, V. M., KACHANOV, Y. S. & KOZLOV, V. V. 1981 The development of spatial wave packets in a boundary layer (in Russian). Preprint 34, Akad. Nauk, USSR, Siberian Div., Inst. of Theor. & Applied Mech., Novosibirsk. (see Mack, 1984).
- GILEV, V. M. & KOZLOV, V. V. 1980 Method of obtaining two- and three-dimensional wave packets in a laminar boundary layer (in Russian). Preprint 2, Akad. Nauk, USSR, Siberian Div., Inst. of Theor. & Applied Mech., Novosibirsk.
- GOLDSTEIN, M. E. 1983 The evolution of Tollmien-Schlichting waves near a leading edge. *J. Fluid Mech.* **127**, 59-81.
- GOLDSTEIN, M. E., SOCKOL, P. M. & SANZ J. 1983 The evolution of Tollmien-Schlichting waves near a leading edge. Part 2. Numerical determination of amplitudes. *J. Fluid Mech.* **129**, 443-453.
- GOLDSTEIN, M. E. 1985 Scattering of acoustic waves into Tollmien-Schlichting waves by small streamwise variations in surface geometry. *J. Fluid Mech.* **154**, 509-529.
- HOOS, J. A. 1990 Boundary-layer receptivity to freestream sound. Master's Thesis, Arizona State University.
- KACHANOV, Y. S. 1984 Development of spatial wave packets in boundary layer. In *Proc. IUTAM Symp. on Laminar-Turbulent Transition*, Novosibirsk, USSR (ed. V. V. Kozlov), pp. 115-123. Springer.

- KENDALL, J. M. 1985 Experimental study of disturbances produced in a pre-transitional laminar boundary layer by weak freestream turbulence. *AIAA Paper No. 85-1695*.
- KENDALL, J. M. 1990 Boundary layer receptivity to freestream turbulence. *AIAA Paper No. 90-1504*.
- KERSCHEN, E. J. 1989 Boundary-layer receptivity. *AIAA Paper No. 89-1109*.
- KERSCHEN, E. J., CHOUDHARI, M. & HEINRICH, R. A. 1989 Generation of boundary layer instability waves by acoustic and vortical freestream disturbances. In *Proc. 3rd IUTAM Symp. on Laminar-Turbulent Transition*. (ed. R. Michel & D. Arnal). Springer.
- KOSORYGIN, V. S. & POLYAKOV, N. F. 1990 Autodestruction of unstable waves in a laminar boundary layer (in Russian). Preprint 11-17, ITPM, Akad. Nauk USSR, Sib. Otd., Novosibirsk.
- LEEHEY, P. & SHAPIRO, P. 1980 Leading-edge effect in laminar boundary layer excitation by sound. In *Proc. IUTAM Symp. on Laminar-Turbulent Transition* (ed. R. Eppler & H. Fasel), pp. 321-331. Springer.
- LIN, N., REED H. L. & SARIC, W. S. 1991 Effect of leading-edge geometry on boundary-layer receptivity to freestream sound. ICASE/NASA LaRC Workshop on Transition and Turbulence, to be published by Springer.
- MACK, L. M. 1984 Boundary-layer linear stability theory. *AGARD Report No. 709* (Special course on stability and transition of laminar flows) VKI, Brussels.
- MACK, L. M. & KENDALL, J. M. 1983 Wave pattern produced by a localized harmonic source in a blasius boundary layer. *AIAA Paper No. 83-0046*.
- MORKOVIN, M. V. 1969 On the many faces of transition. In *Viscous Drag Reduction* (ed. C. S. Wells), pp.1-31. Plenum.
- NISHIOKA, M. & MORKOVIN, M. V. 1986 Boundary-layer receptivity to unsteady pressure gradients: experiments and overview. *J. Fluid Mech.* **171**, 219-261.
- PAREKH, D. E., PULVIN, P. & WLEZIEN, R. W. 1991 Boundary layer receptivity to convected gusts and sound. In *Proc. ASME-JSME Symp. on Boundary Layer Stability and Transition to Turbulence*.
- PRANDTL L. 1928 Motion of fluids with very little viscosity. *N.A.C.A. TM No. 452*.

- RADEZTSKY, R. H., KOSORYGIN, V. S. & SARIC, W. S. 1991 Control of T-S waves with freestream sound and 2-D roughness. *Bull. Am. Phys. Soc.* **36**, No. 10, pp. 2629.
- SARIC, W. S. 1989 The ASU unsteady wind tunnel. *College of Engineering and Applied Science Report CEAS-CR-R-89030*, Arizona State University.
- SARIC, W. S. 1990 Low-speed experiments: requirements for stability measurements. In *Instability and Transition*, vol. 1. (ed. M. Y. Hussaini & R. G. Voight), pp. 162-174. Springer.
- SARIC, W. S., HOOS, J. A. & KOHAMA, Y. 1990 Boundary-layer receptivity: Part 1. Freestream sound and 2-D roughness strips. *College of Engineering and Applied Science Report CEAS-CR-R-90191*, Arizona State University.
- SARIC, W. S., HOOS, J. A. & RADEZTSKY, R. H. 1991 Boundary-layer receptivity of sound with roughness. In *Proc. ASME-JSME Symp. on Boundary Layer Stability and Transition to Turbulence*, vol. 114., pp. 17-22.
- SARIC, W. S., TAKAGI, S. & MOUSSEUX, M. 1988 The ASU Unsteady Wind Tunnel and fundamental requirements for freestream turbulence measurements. *AIAA Paper No.* 88-0053.
- SCHLICHTING, H. 1933 Zur entstehung der turbulenz bei der plattenströmung, Nach. Gesell. d. Wiss. z. Gött, *M.P.K.*, pp. 181-208.
- SCHLICHTING, H. 1935 Amplitudenverteilung und energiebilanz der kleinen störungen bei der plattenströmung, Nach. Gesell. d. Wiss. z. Gött, *M.P.K.*, Vol. I, pp. 47-48.
- SCHUBAUER, G. B. & SKRAMSTAD, H. K. 1947a Laminar boundary layer oscillations and stability of laminar flow. *J. Aero. Sci.* **14**, pp. 69-78.
- SCHUBAUER, G. B. & SKRAMSTAD, H. K. 1947b Laminar boundary layer oscillations and transition on a flat plate. *J. Res. NBS* **38**, RP1722.
- TADJFAR, M. 1990 Receptivity of a laminar boundary layer to the interaction of a three-dimensional roughness element with time-harmonic free-stream disturbances. PhD Dissertation, Ohio State University.
- TOLLMIE, W. 1931 The production of turbulence, *N.A.C.A. TM No.* 609.
- WLEZIEN, R. W. 1989 Measurement of boundary-layer receptivity at suction surfaces. *AIAA Paper No.* 89-1006.

WLEZIEN, R. W., PAREKH, D. E. & ISLAND, T. C. 1990 Measurement of acoustic receptivity at leading edges and porous strips. *Appl. Mech. Rev.*, Vol. 43, No. 5, part 2, May 1990.

APPENDIX A
FACILITY

A.1. Wind Tunnel

The ASU Unsteady Wind Tunnel is a low-speed, low-turbulence, closed-return wind tunnel. Originally located at the National Bureau of Standards in Gaithersburg, Maryland, the wind tunnel was designed by Dr. Philip Klebanoff. After being moved to ASU in 1984, the facility was reconstructed and became operational in 1987. Two unique aspects of the wind tunnel are the unsteady operational mode (not used in this experiment) and extremely low turbulence levels.

The wind tunnel test section is 1.4 m square and 5 m long. Drawings of the facility are given in Figure 3.1. Maximum freestream speed is 36 m/s, provided by a 150 hp variable-speed DC motor. The fan diameter is 1.8 m, with 9 blades and 11 stators. Both the fan motor and the test section are secured to 0.3-m-thick concrete slabs isolated from the rest of the building by a damping material. The contraction cone is a symmetric, fifth-order polynomial curve structure with an area ratio of 5.3 to 1.

All aspects of construction of the ASU Unsteady Wind Tunnel have been tailored toward reducing mean flow turbulence levels. The flow passes through a 76-mm section of aluminum honeycomb after the last turn before the contraction cone. Downstream of the honeycomb, a series of seven stainless steel screens further reduce turbulence before the flow enters the settling chamber and contraction cone. The screens are 2.7 m by 3.7 m (9' by 12') with an open air ratio of 0.65. The last two are seamless. All seven screens were removed, cleaned, and replaced in the summer of 1991, just prior to the beginning of these experiments. See Table 1 for mean flow turbulence levels.

Table 1: Freestream Turbulence Levels

0.1 Hz–1 kHz Bandpass			2 Hz–1 kHz Bandpass		
U_∞ (m/s)	Streamwise Fluctuations $ u' $	Transverse Fluctuations $ v' $	U_∞ (m/s)	Streamwise Fluctuations $ u' $	Transverse Fluctuations $ v' $
5	0.069%	0.018%	5	0.018%	0.007%
10	0.088%	0.016%	10	0.030%	0.014%
15	0.085%	0.018%	15	0.038%	0.014%
25	0.067%	0.032%	25	0.092%	0.035%
30	0.054%	0.026%	30	0.095%	0.040%

A.2. Flat-Plate Model

The flat-plate model used for this experiment has a span of 1.4 m, a chord of 3.7 m, and is 21 mm thick. It is made of two 6061-T6 aluminum sheets sandwiching 19-mm paper honeycomb. The leading edge is an ellipse with aspect ratio 67:1 and a major axis of 0.34 m. The juncture between the leading edge and the plate is filled with bondo and has been wet-sanded and polished to minimize any discontinuities in the surface. The surface of the flat plate is also polished to a near-mirror finish.

The flat plate is mounted in the test section with a series of 10 brackets. These brackets provide fine adjustment of the model at several streamwise locations to ensure a zero-pressure gradient condition on the model. The pressure gradient is verified by taking mean-flow boundary-layer profiles and matching the shape factor with 2.59. Also, a trailing edge flap, 0.35 m long, is set at an angle of 4.5° to ensure that the attachment point is not on the testing side of the model.

Table 2: Traverse Specifications

	$x(\text{chord})$	$y(\text{normal})$	$z(\text{span})$
Total Travel	1.25 m	100 mm	180 mm
Minimum Step	240 μm	12 μm	100 μm

A.3. Three-Dimensional Traverse

A three-dimensional traversing system is used to map the disturbance field created by the applied roughness element. The traversing system is located outside the tunnel and is powered by three Slo-Syn stepper motors and their respective controllers. Voltage pulses are sent from the Concurrent (Masscomp) 5600, 8 channel, 500 kHz D/A board to the controllers, and the controllers return an actual distance moved after each step. During a testing run, all traverse movement is controlled and monitored by the data acquisition codes.

In the x -direction, the stepper motor is geared to a drive train moving a carriage which is supported by two Thompson rails. The instrumentation sting, a 45° forward-swept carbon-carbon composite arm, pushes open and pulls closed a horizontal zipper in a plexiglass window. In the z -direction, the stepper motor is geared to two precision lead screws. The plexiglass window slides in the z -direction and is moved by the instrumentation sting. A single precision lead screw is turned by the y stepper motor, moving the sting through the boundary layer. The total ranges of motion and minimum step sizes are listed in Table 2.

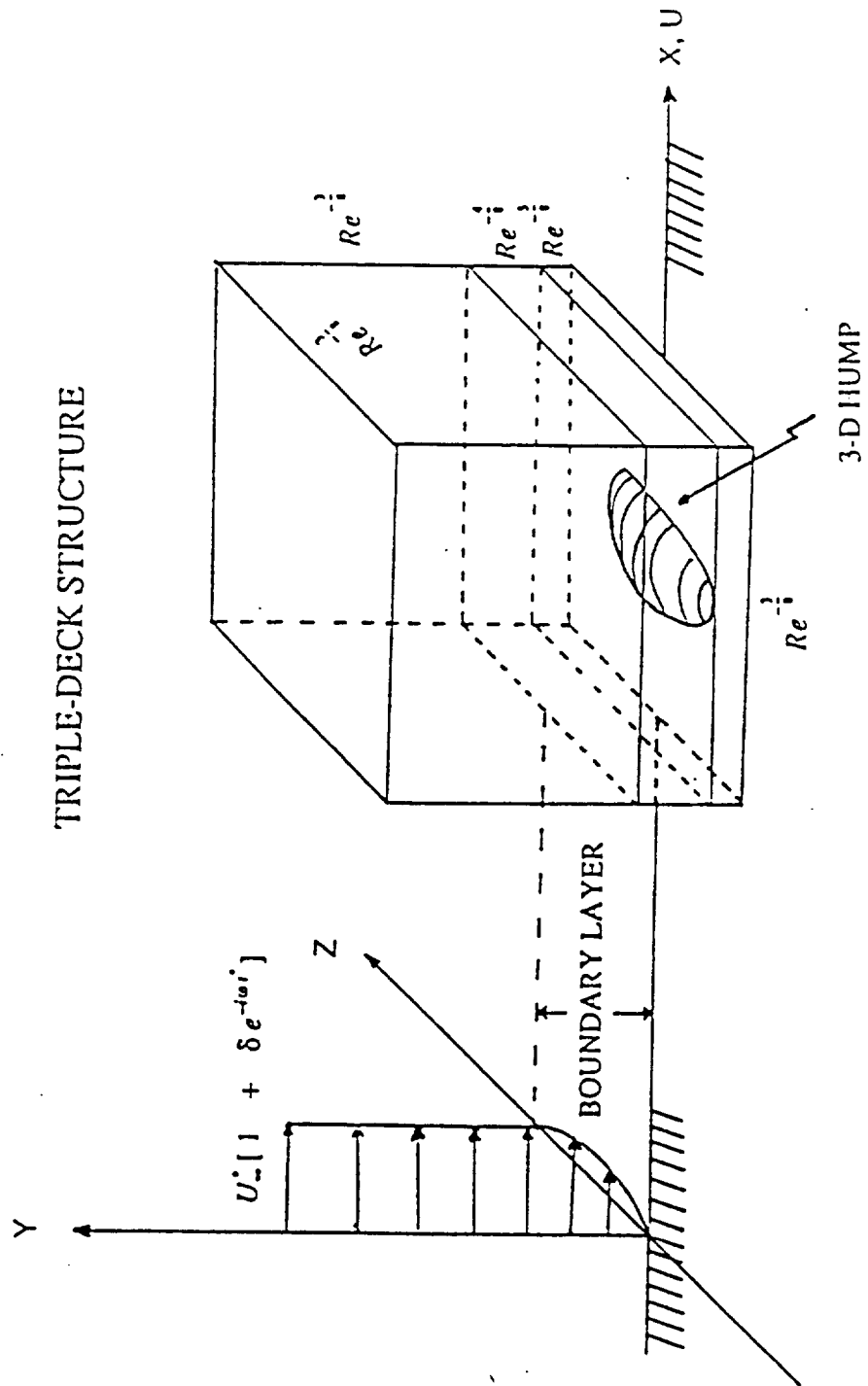


Figure 2.1: Triple-deck structure. (Tadjfar, 1990)

Predicted Effect of 3-D Roughness (Choudhari & Kerschen, 1990)

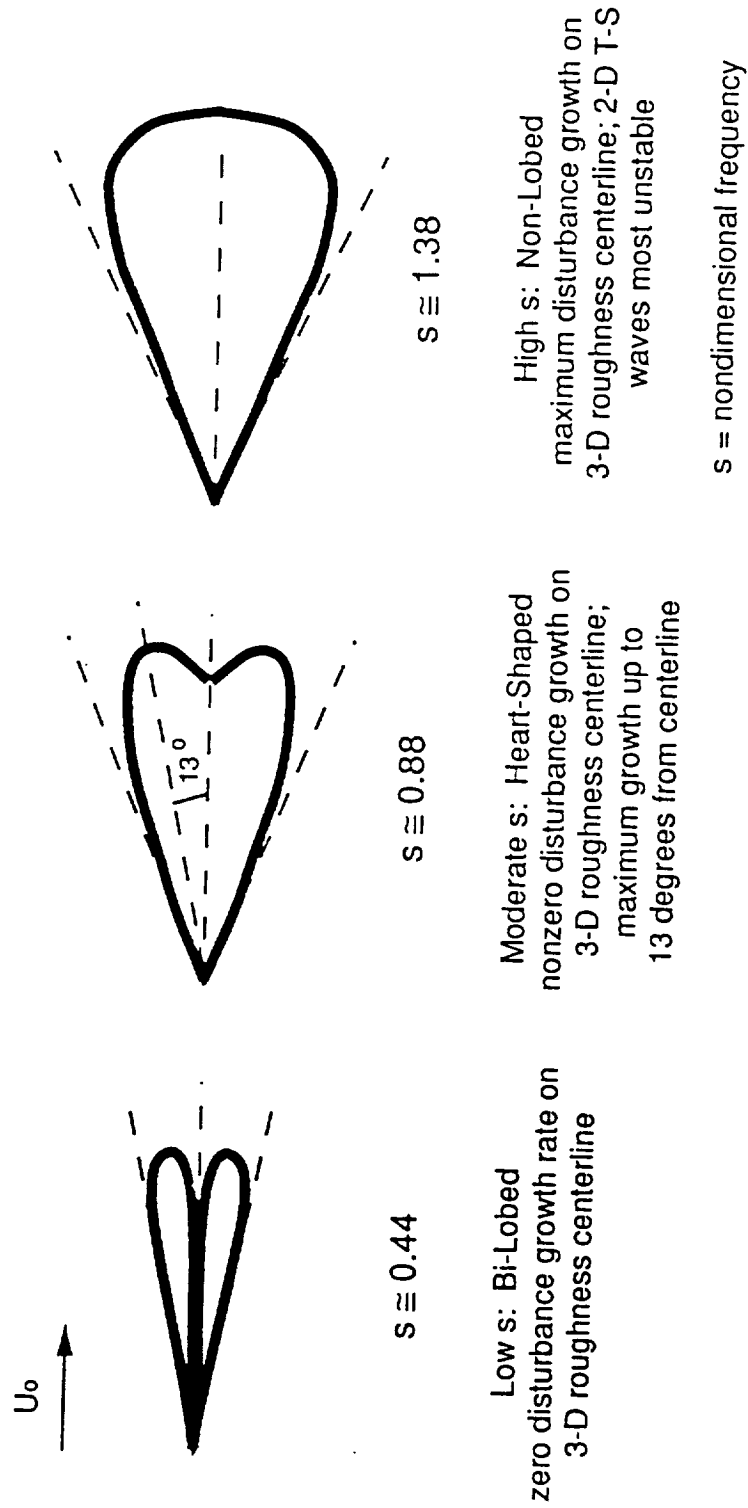


Figure 2.2: 3-D roughness disturbance-field characteristics.

6 Circular Layers of 40 μm tape

Designed to Approximate
a Gaussian Distribution:

$$h = H e^{-4r^2/D^2}$$

$$D = 25 \text{ mm}$$

$$H = 240 \mu\text{m}$$

$$D = \frac{2 \lambda_{\text{TS}}}{\pi}$$

H is on the order
of the lower viscous
deck
as defined by
Triple-Deck Theory

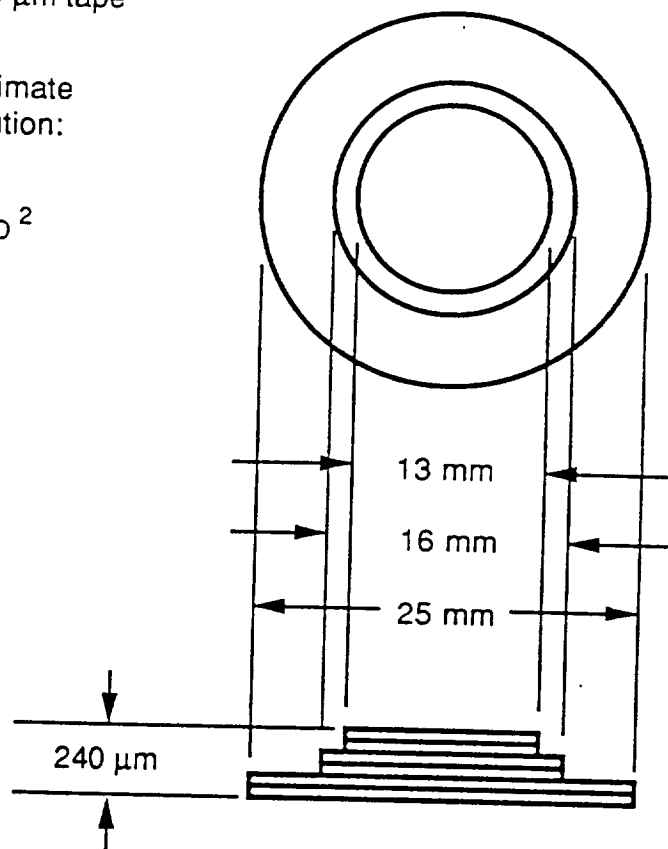


Figure 2.3: 3-D roughness element.

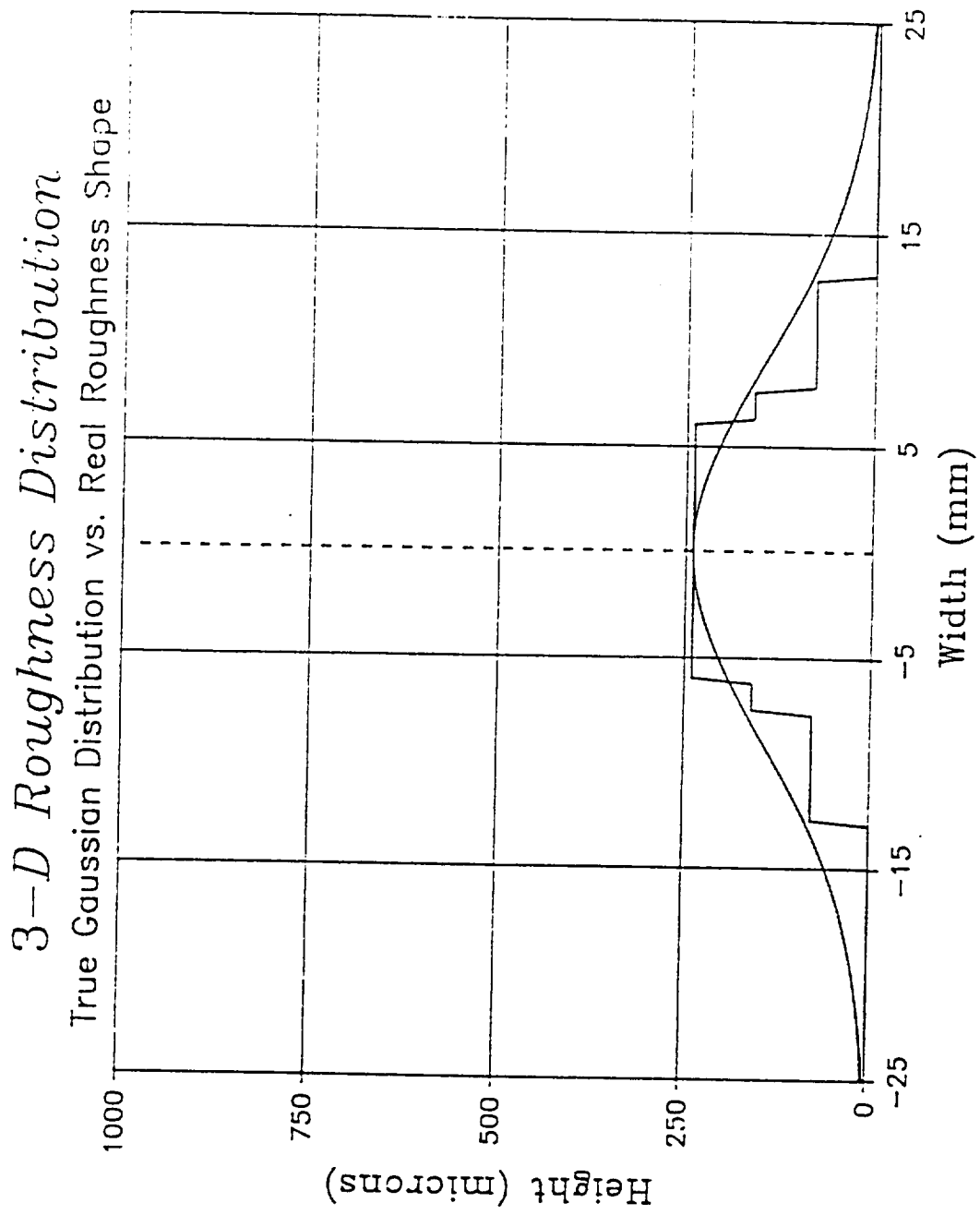


Figure 2.4: Comparison of 3-D roughness and Gaussian distribution.

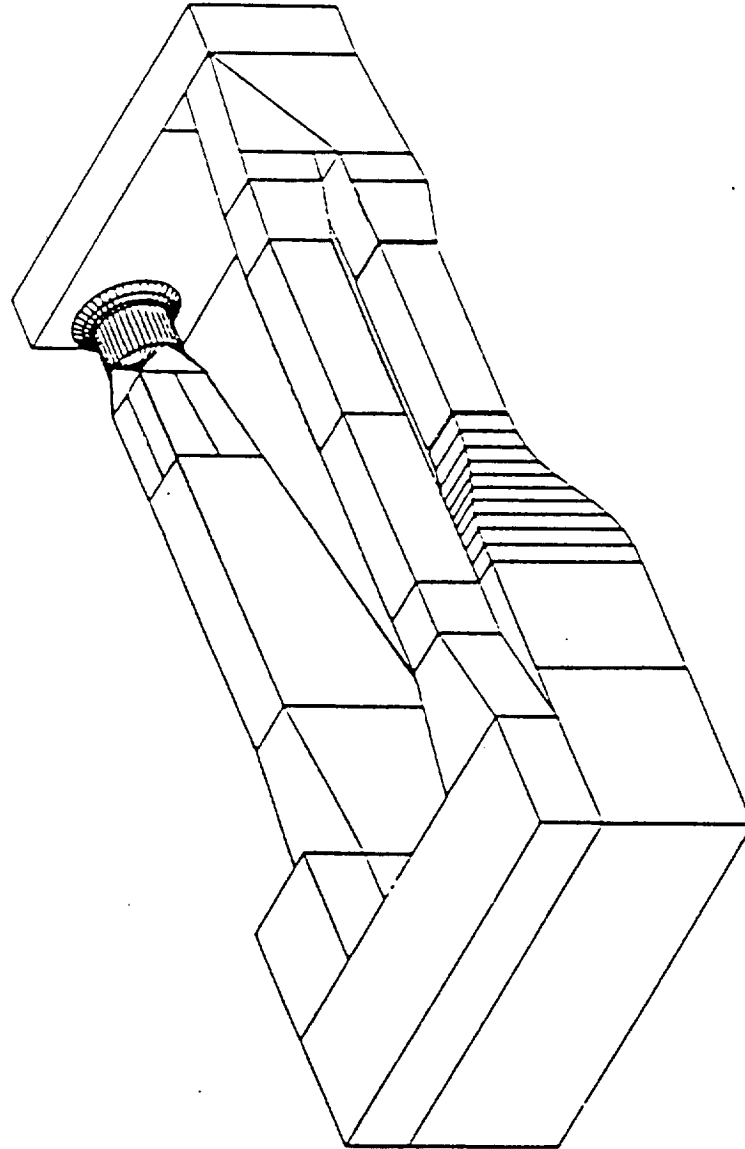


Figure 3.1: ASU Unsteady Wind Tunnel.

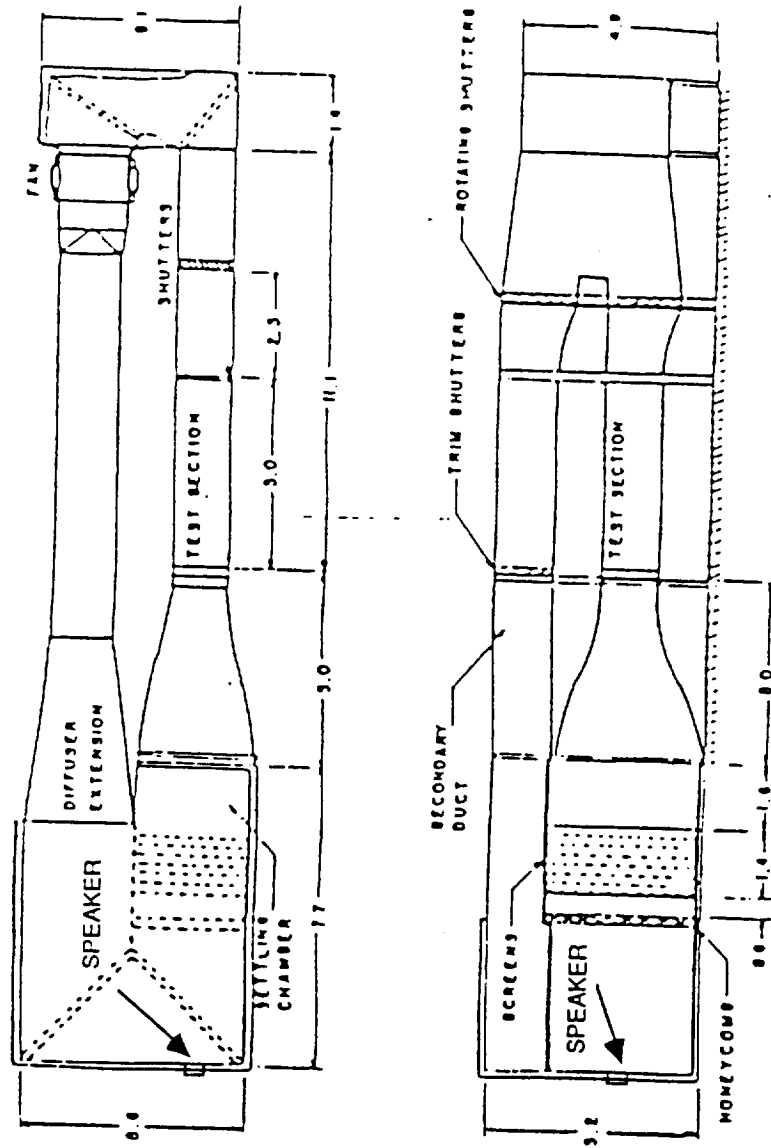


Figure 3.2: Speaker location in wind tunnel. (All dimensions in meters.) (Sarić, 1989)

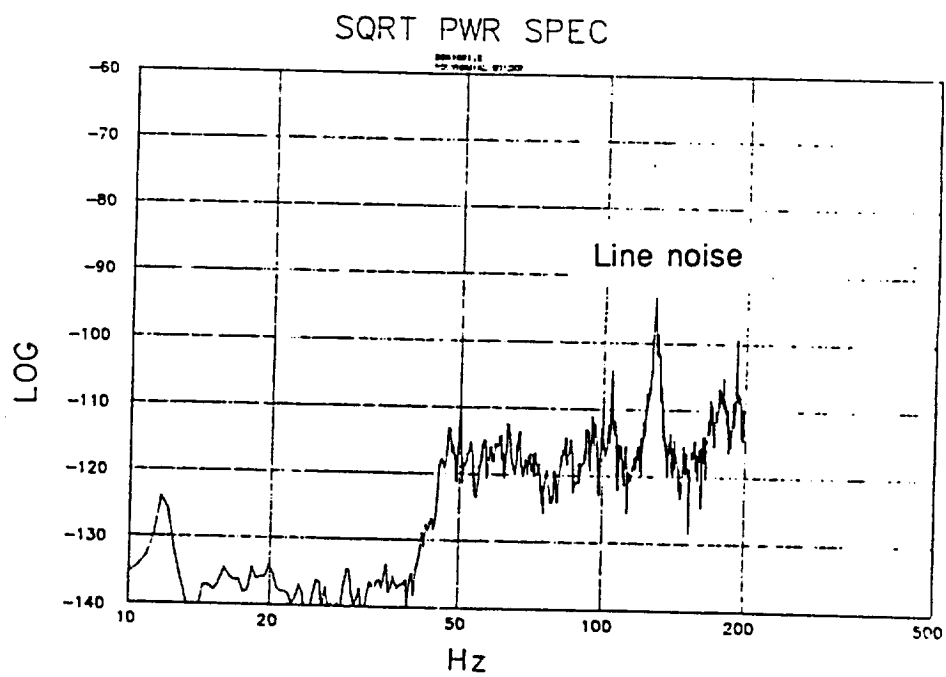
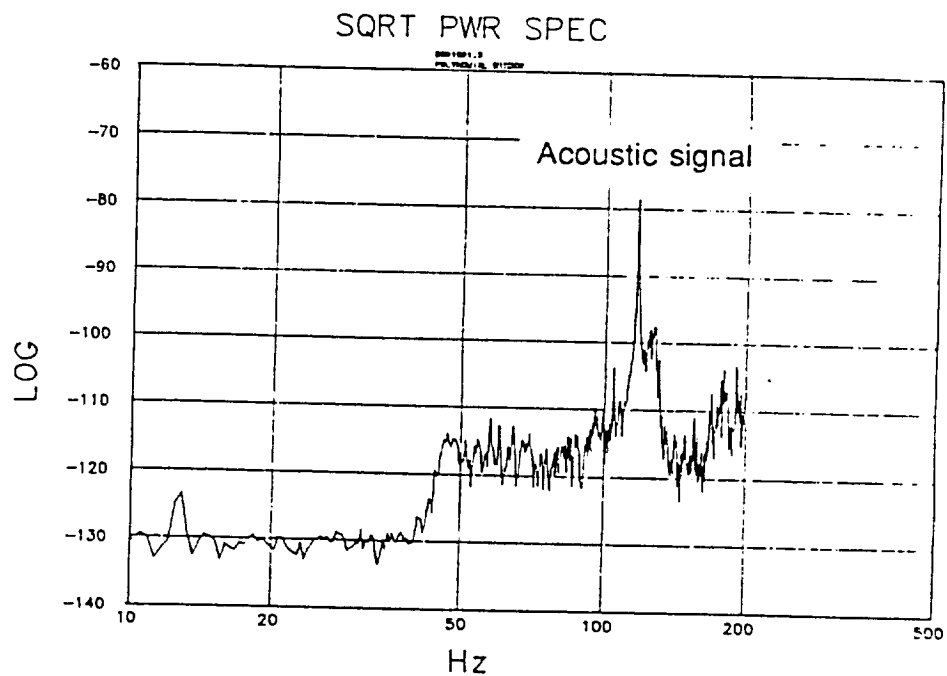
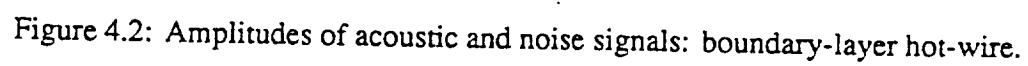


Figure 4.1: Amplitudes of acoustic and noise signals: freestream hot-wire.



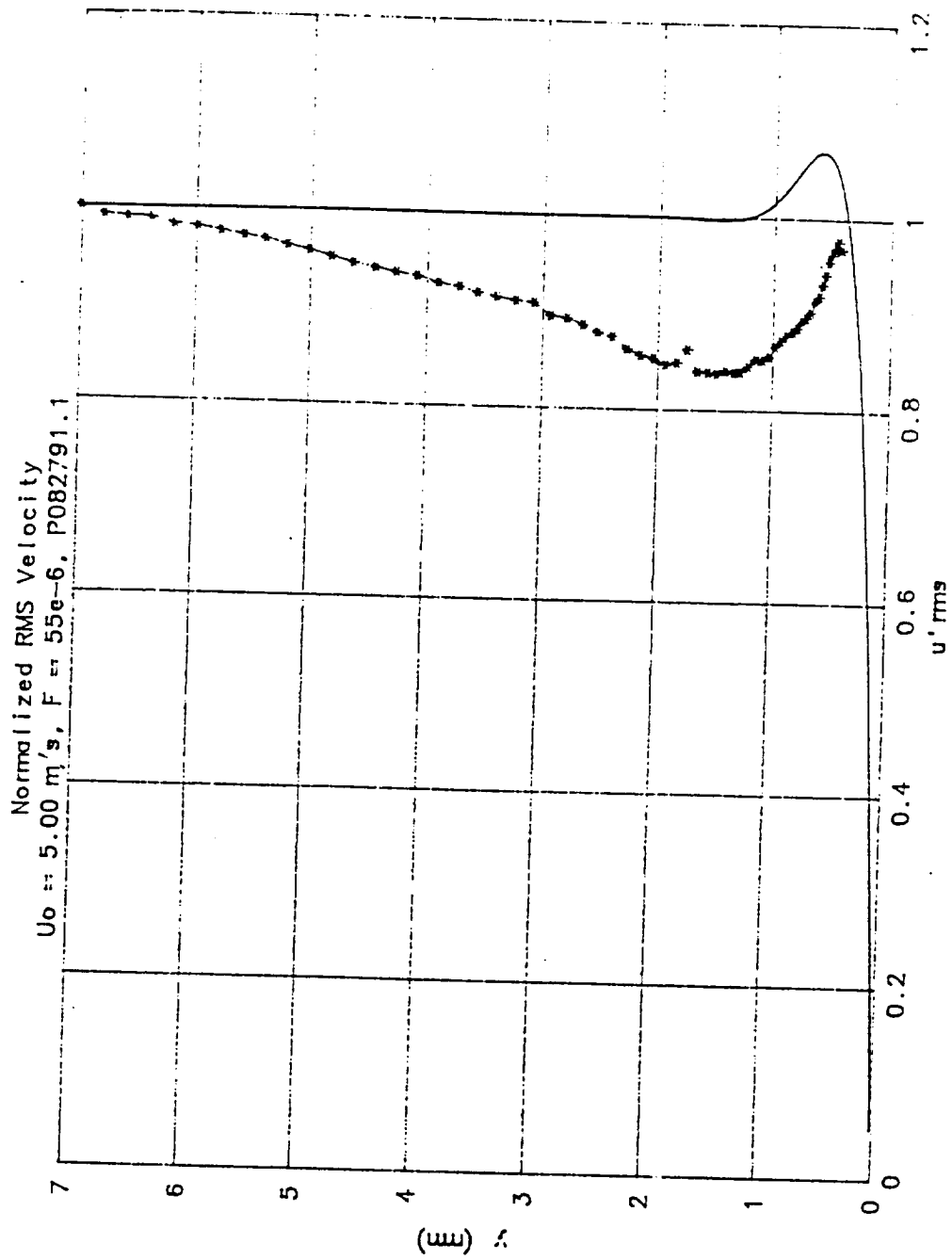
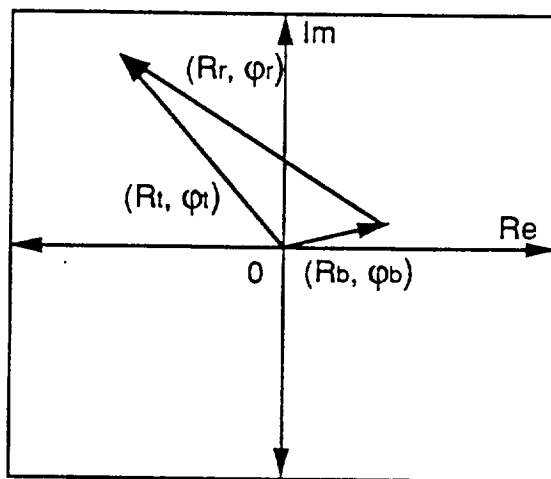


Figure 4.3: Direct measurement of Stokes layer compared with theoretical profile.



- | | |
|--------------------|---|
| (R_b, φ_b) | Background Signal (without 3-D roughness element) |
| (R_t, φ_t) | Total Signal (with 3-D roughness element) |
| (R_r, φ_r) | 3-D Roughness T-S Signal |

Figure 4.4: Complex plane signal subtraction technique.

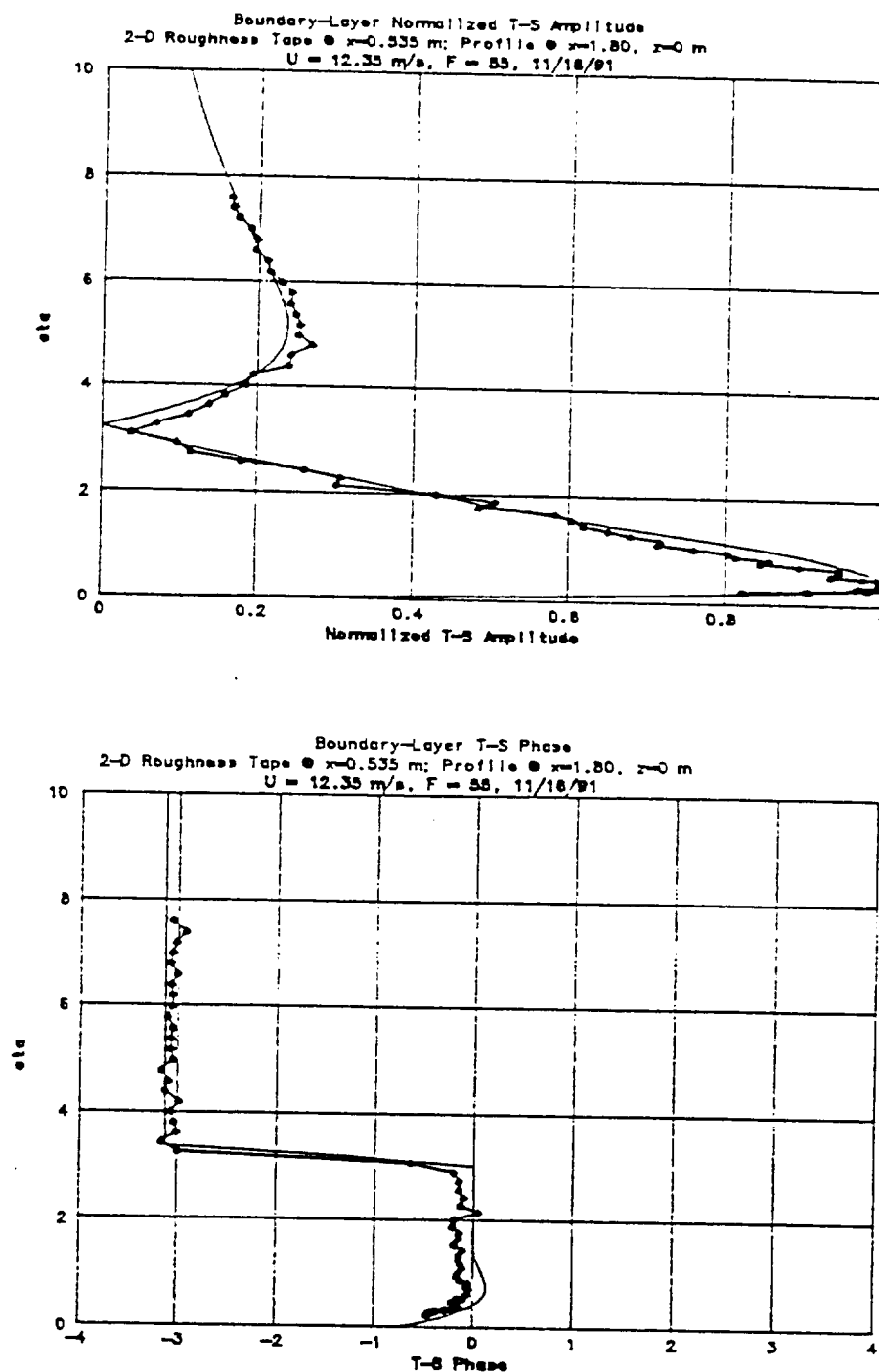


Figure 4.5: Roughness signal discrimination technique applied to 2-D T-S wave. (Data plotted with theoretical 2-D T-S curve.)

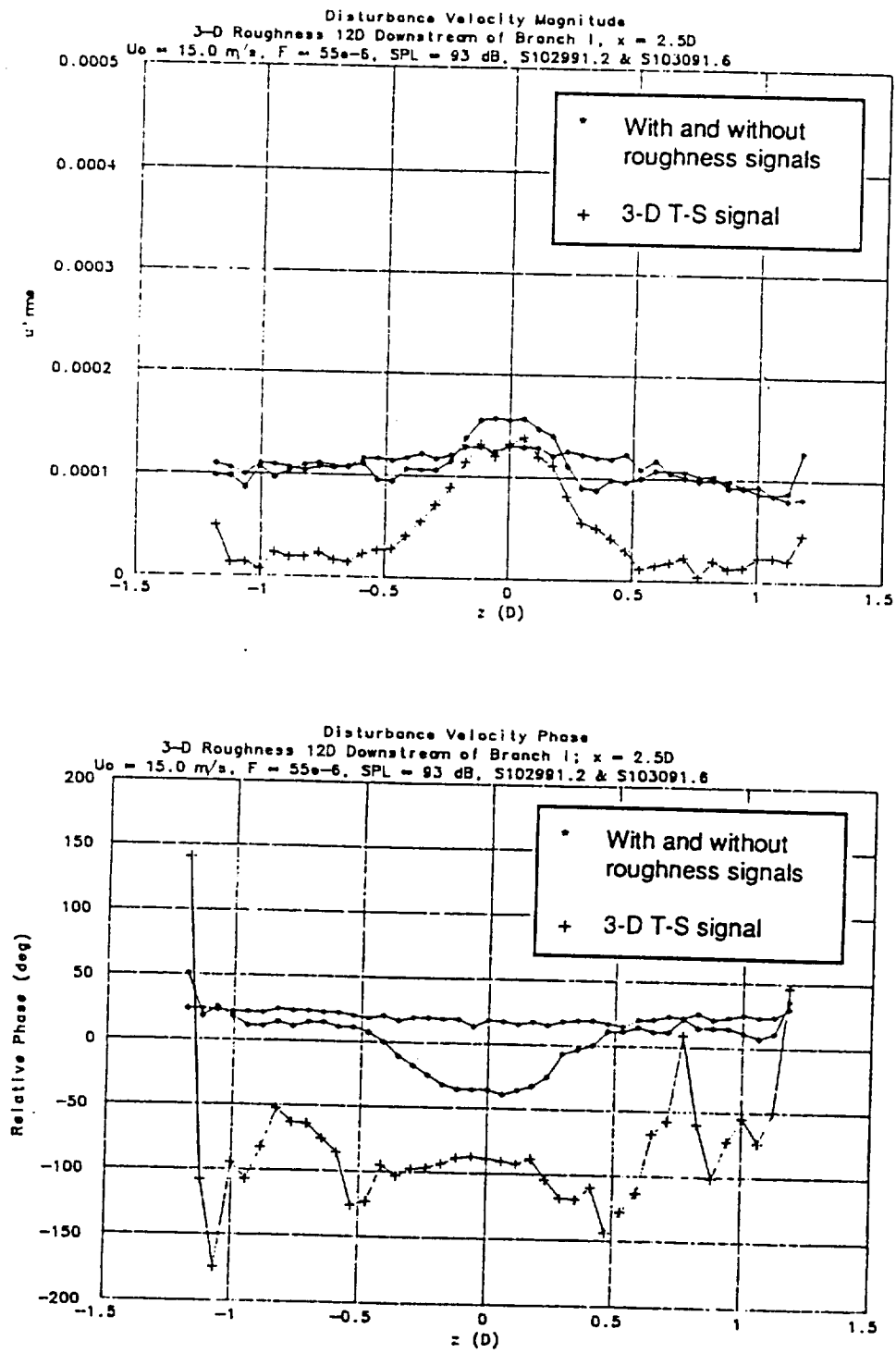


Figure 4.6: Example of 3-D roughness T-S signal discrimination.

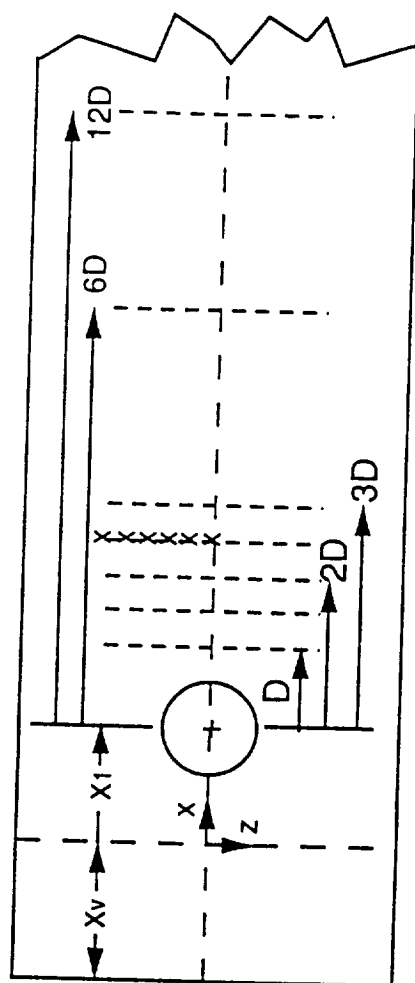


Figure 4.7: Measurement locations: 3-D roughness at Branch I.

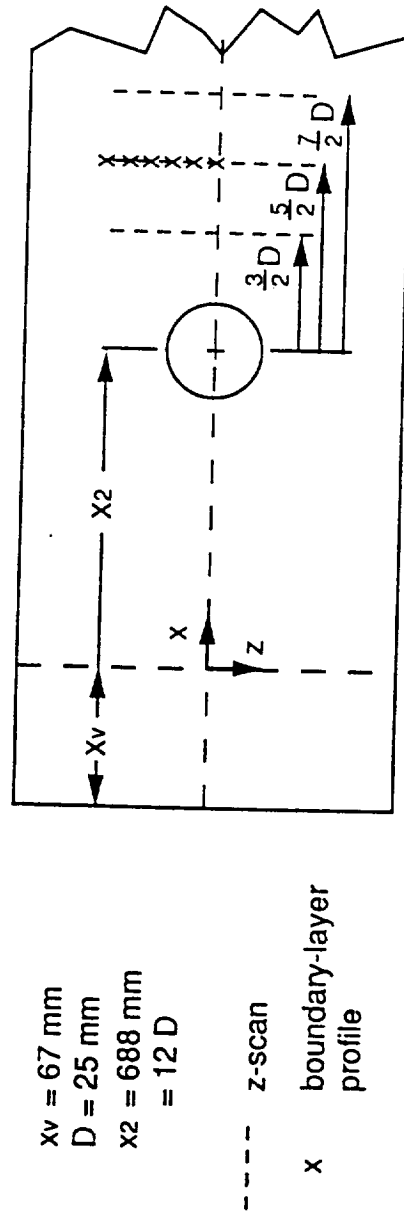


Figure 4.8: Measurement locations: 3-D roughness downstream of Branch I.

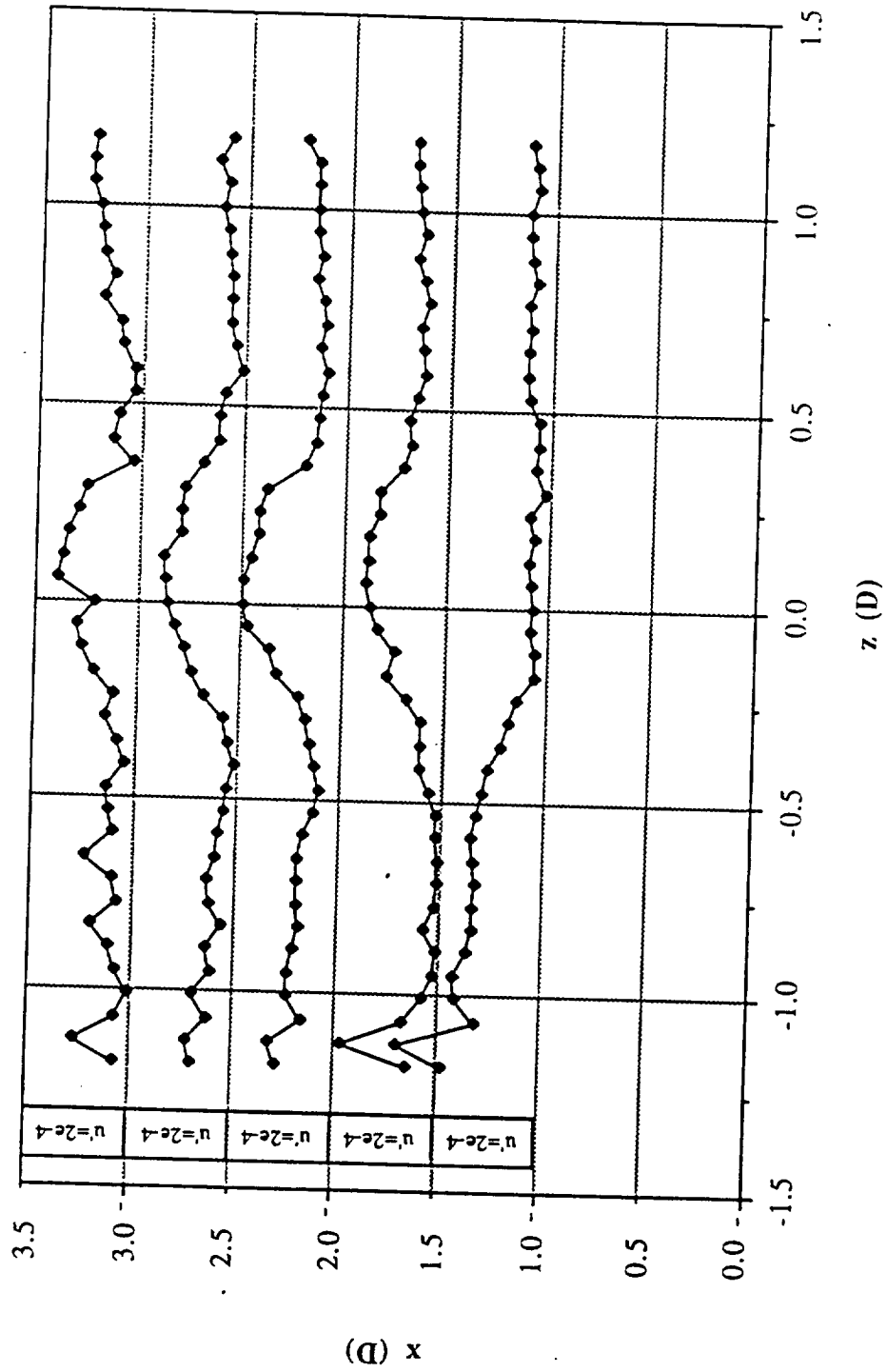


Figure 6.1: Spanwise and streamwise variation of u' amplitude: 3-D roughness element at Branch I; $x = D$ to $\pi = 3D$; $U(y) = 0.47$; $SPL = 93$ dB.

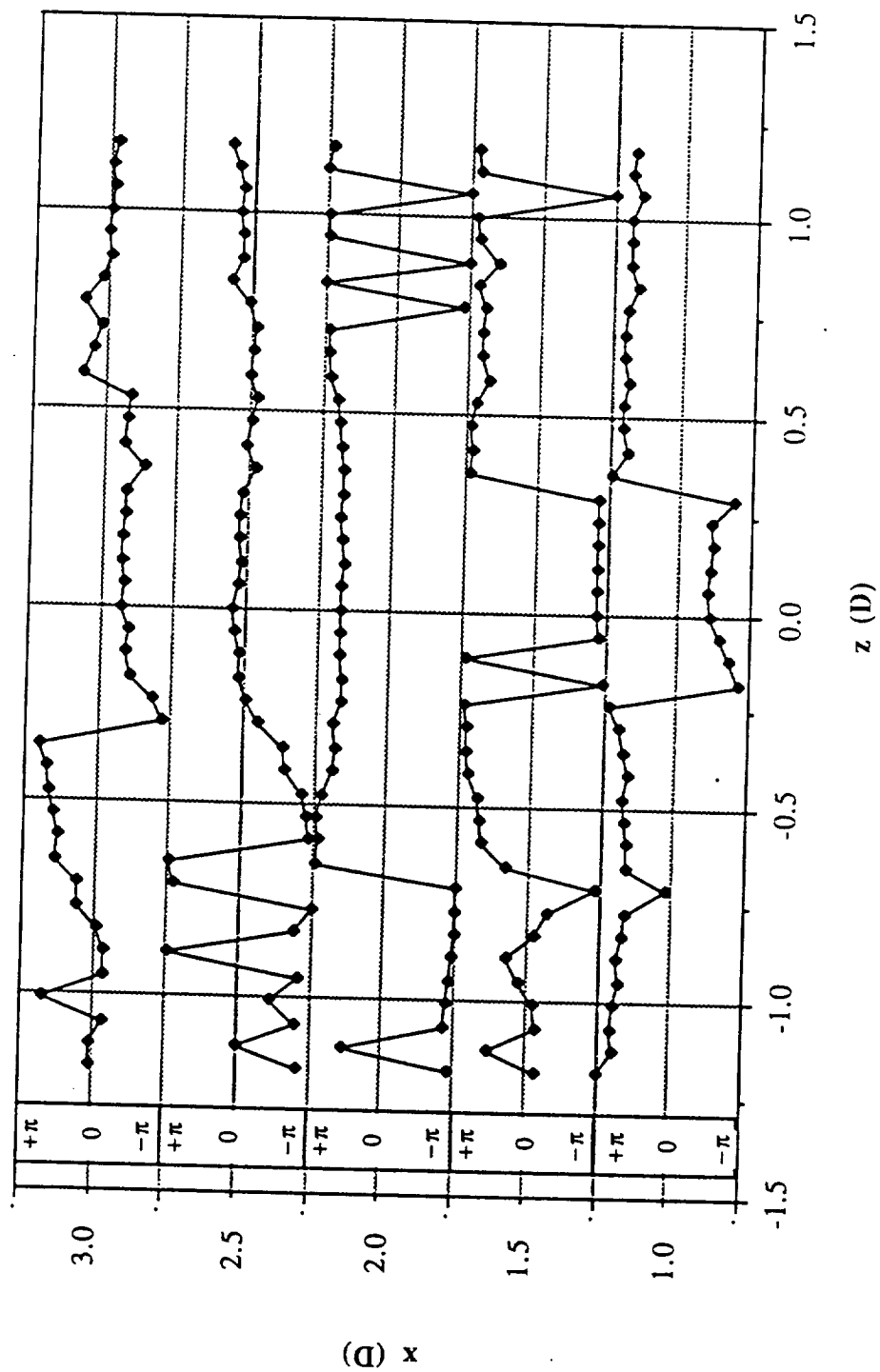


Figure 6.2: Spanwise and streamwise variation of u' phase: 3-D roughness element at Branch I; $x = D$ to $x = 3D$; $U(y) = 0.47$; $SPL = 93$ dB.

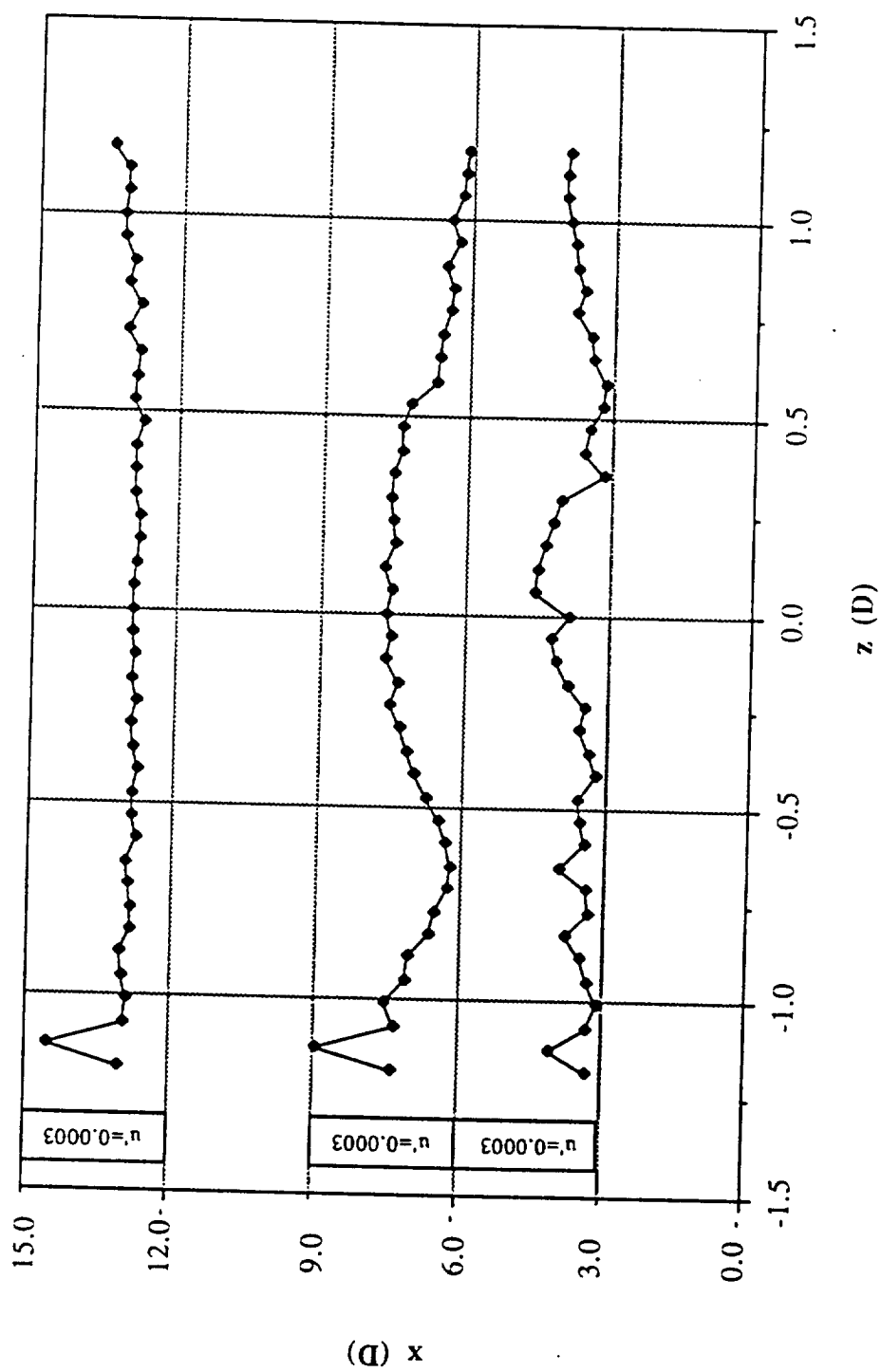


Figure 6.3: Spanwise and streamwise variation of u' amplitude: 3-D roughness element at Branch I; $x = 3D$ to $x = 12D$; $U(y) = 0.47$; $SPL = 93$ dB.

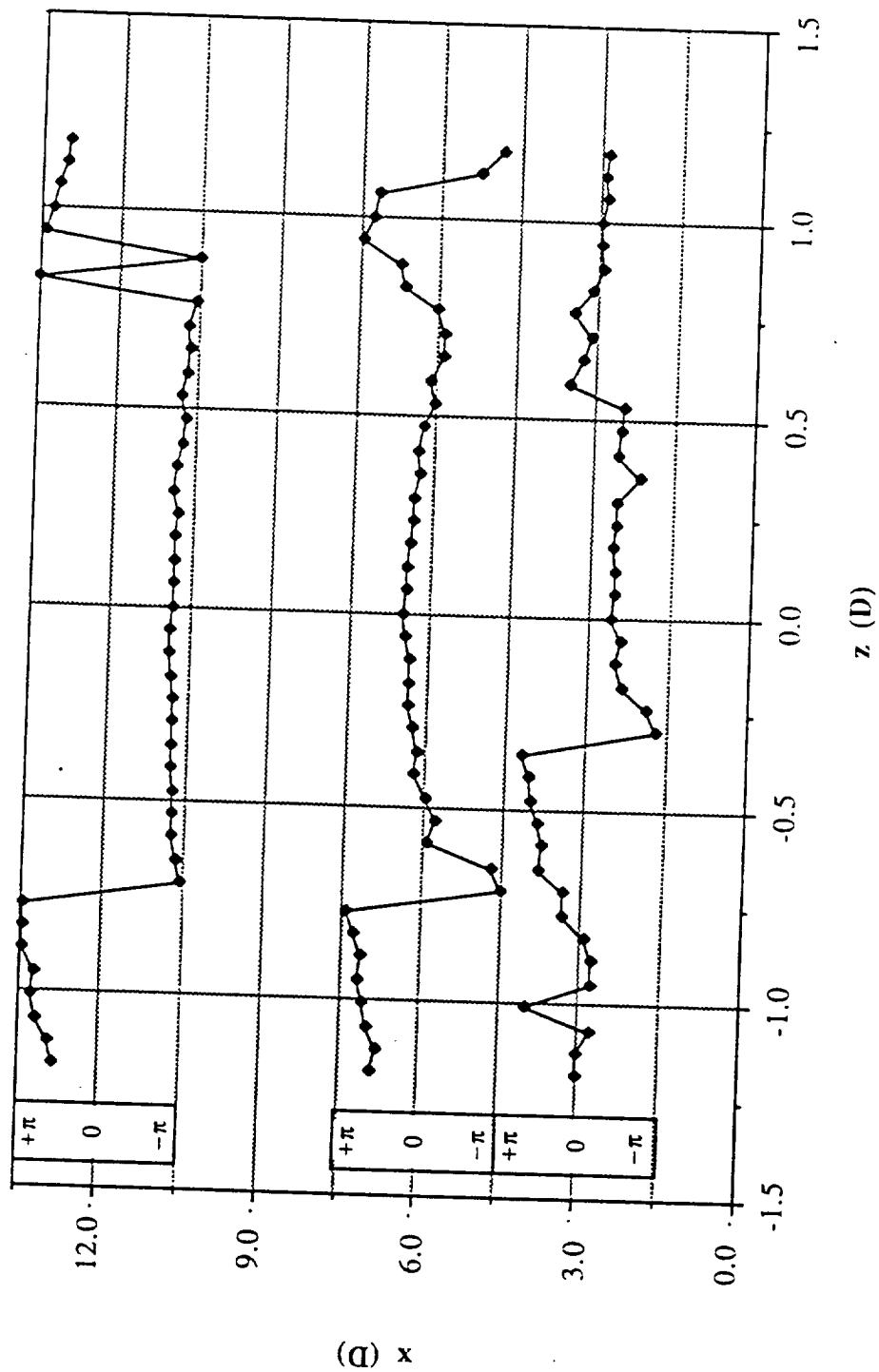


Figure 6.4: Spanwise and streamwise variation of u' phase: 3-D roughness element at Branch I; $x = 3D$ to $x = 12D$; $U(y) = 0.47$; $SPL = 93$ dB.

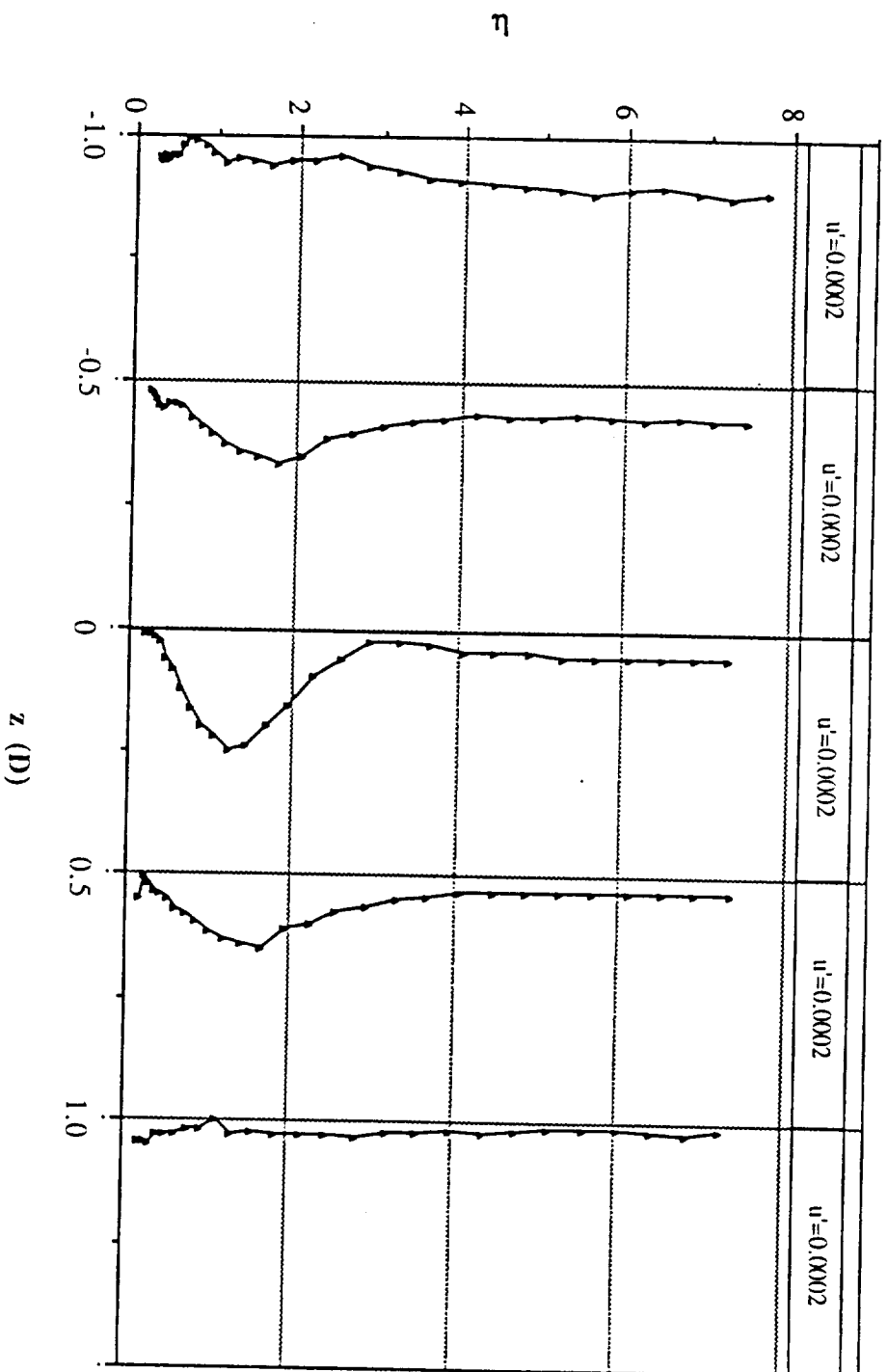


Figure 6.5: Spanwise and normal variation of u' amplitude: 3-D roughness element at Branch I; $z = -D$ to $z = D$; $x = 2.5D$; $SPL = 93$ dB.

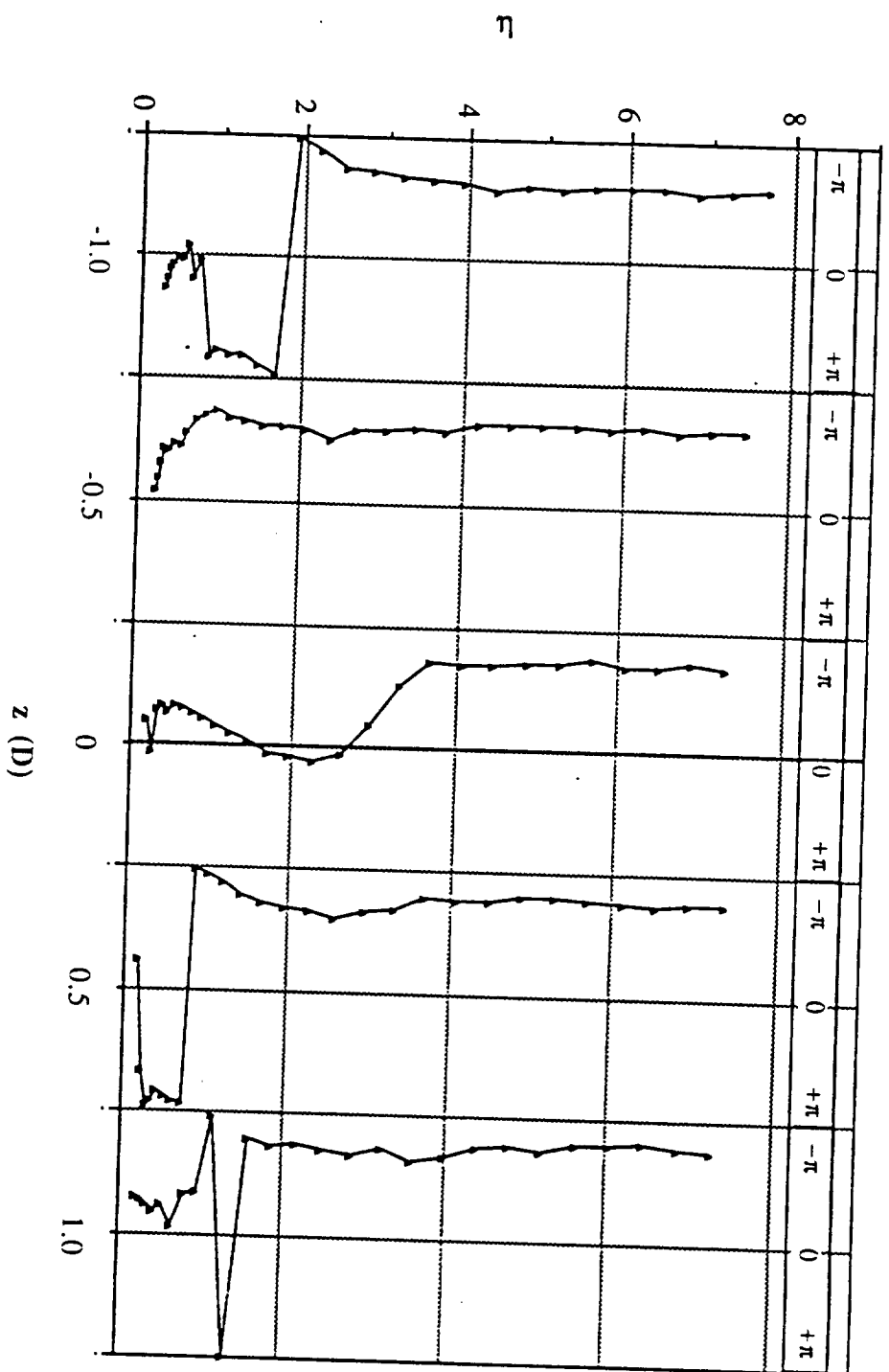


Figure 6.6: Spanwise and normal variation of u' phase: 3-D roughness element at Branch I; $z = -D$ to $z = D$; $x = 2.5D$; $SPL = 93$ dB.

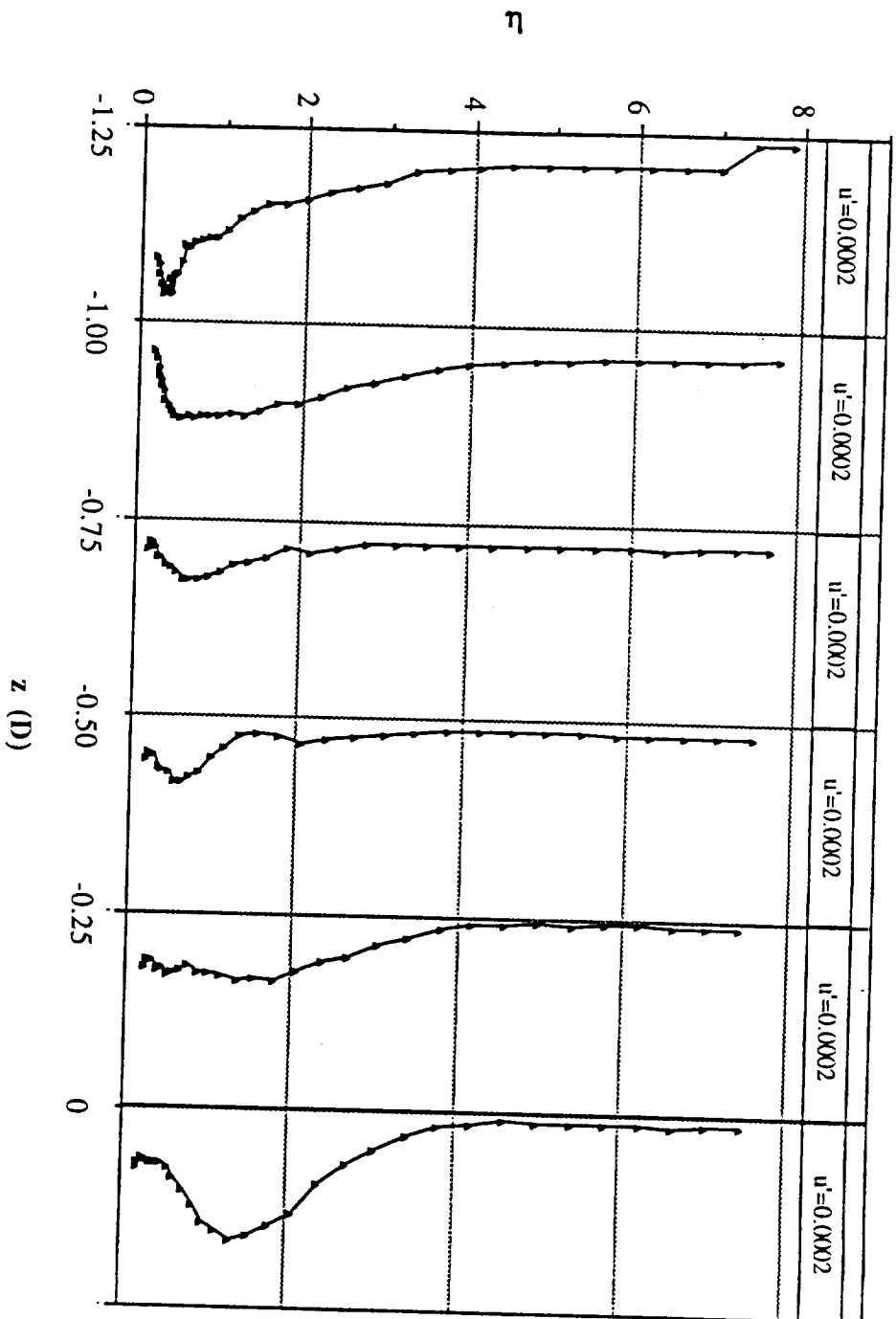


Figure 6.7: Spanwise and normal variation of u' amplitude: 3-D roughness element at Branch I; $z = -1.25D$ to $z = 0$; $x = 2.5D$; $SPL = 93$ dB.

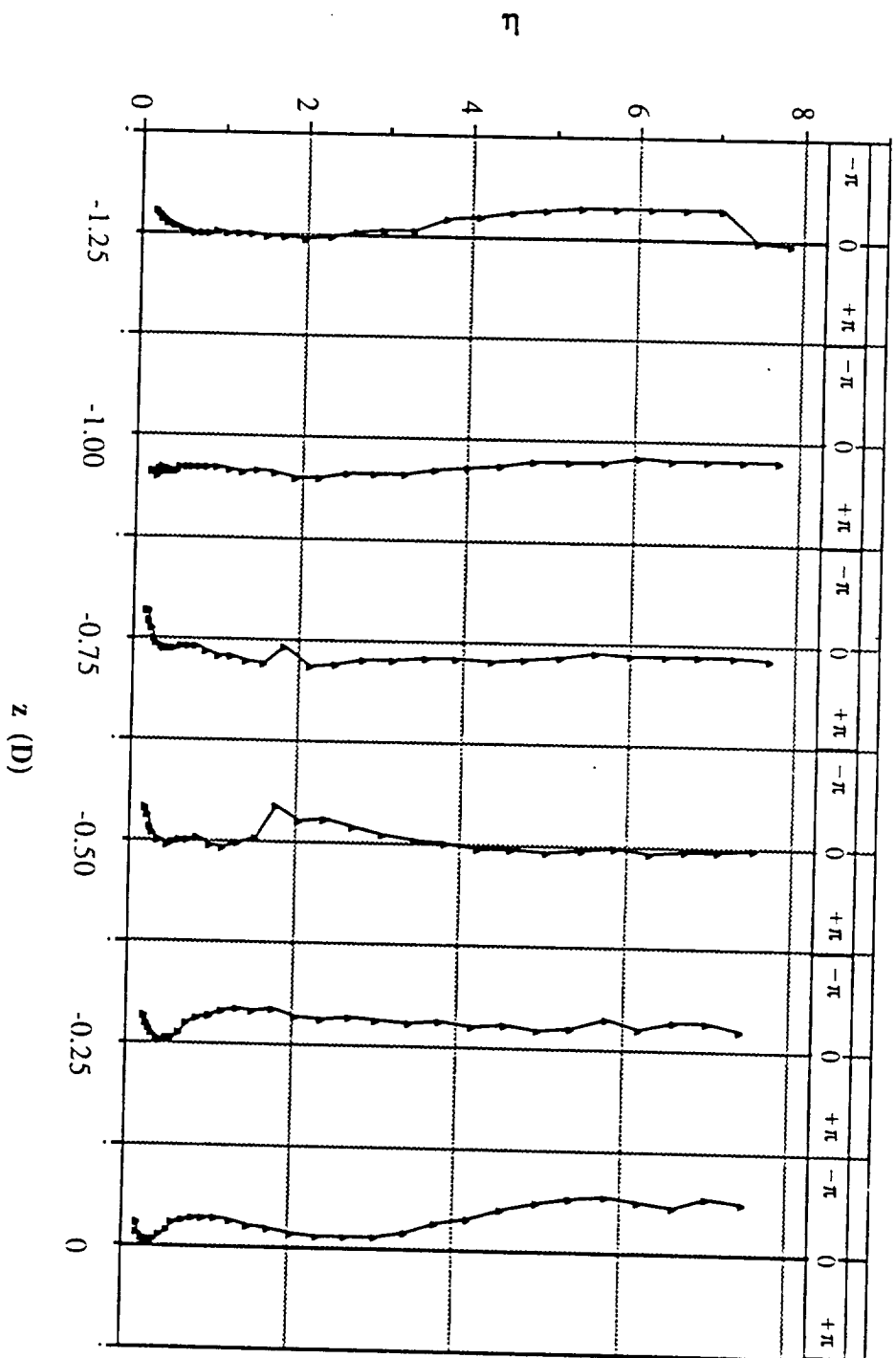


Figure 6.8: Spanwise and normal variation of u' phase: 3-D roughness element at Branch I; $z = -1.25D$ to $z = 0$; $x = 2.5D$; $SPL = 93$ dB.

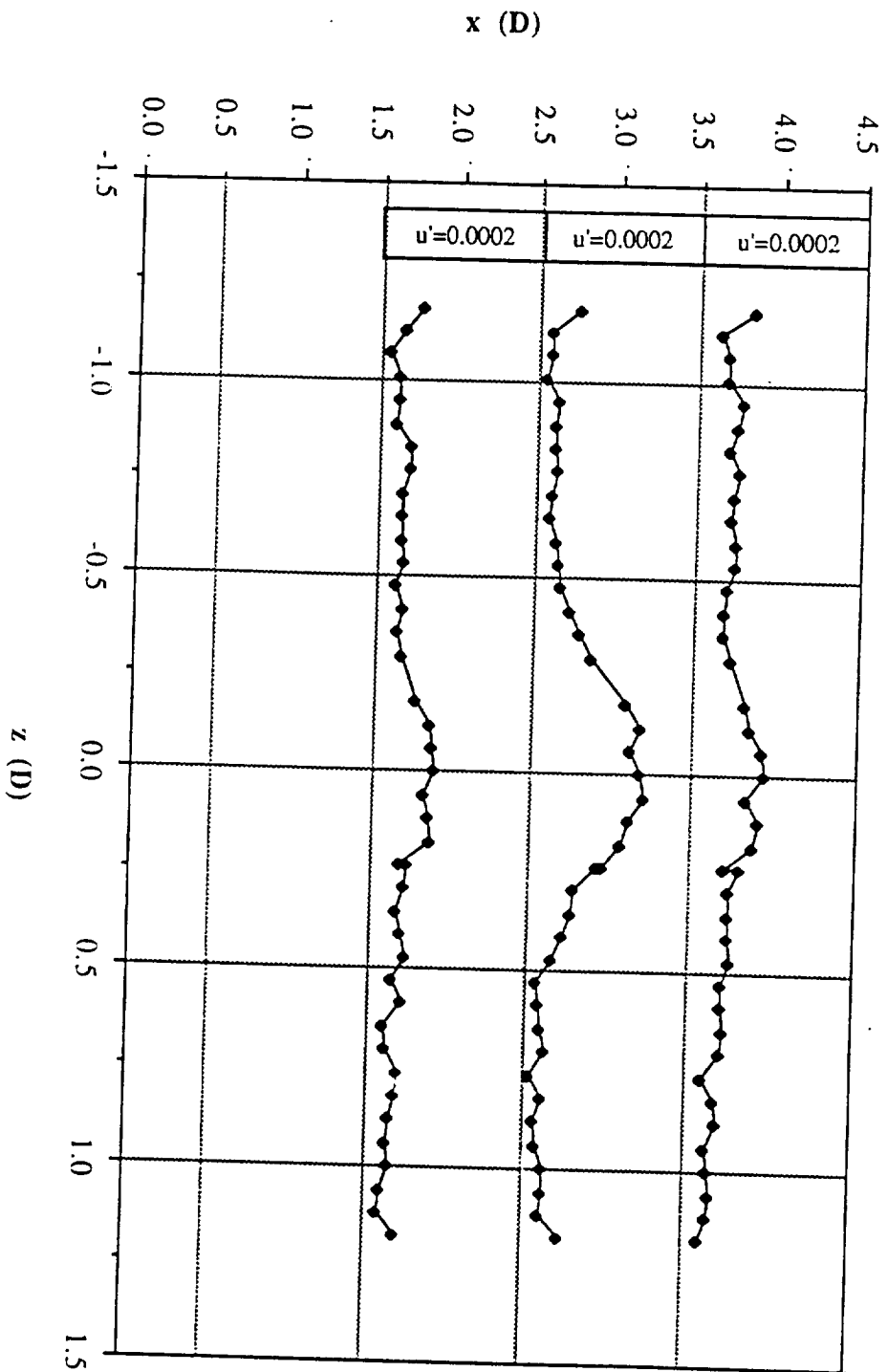


Figure 6.9: Spanwise and streamwise variation of u' amplitude: 3-D roughness element 12D downstream of Branch I; $x = 1.5D$ to $x = 3.5D$; $U(y) = 0.40$; $SPL = 93$ dB.

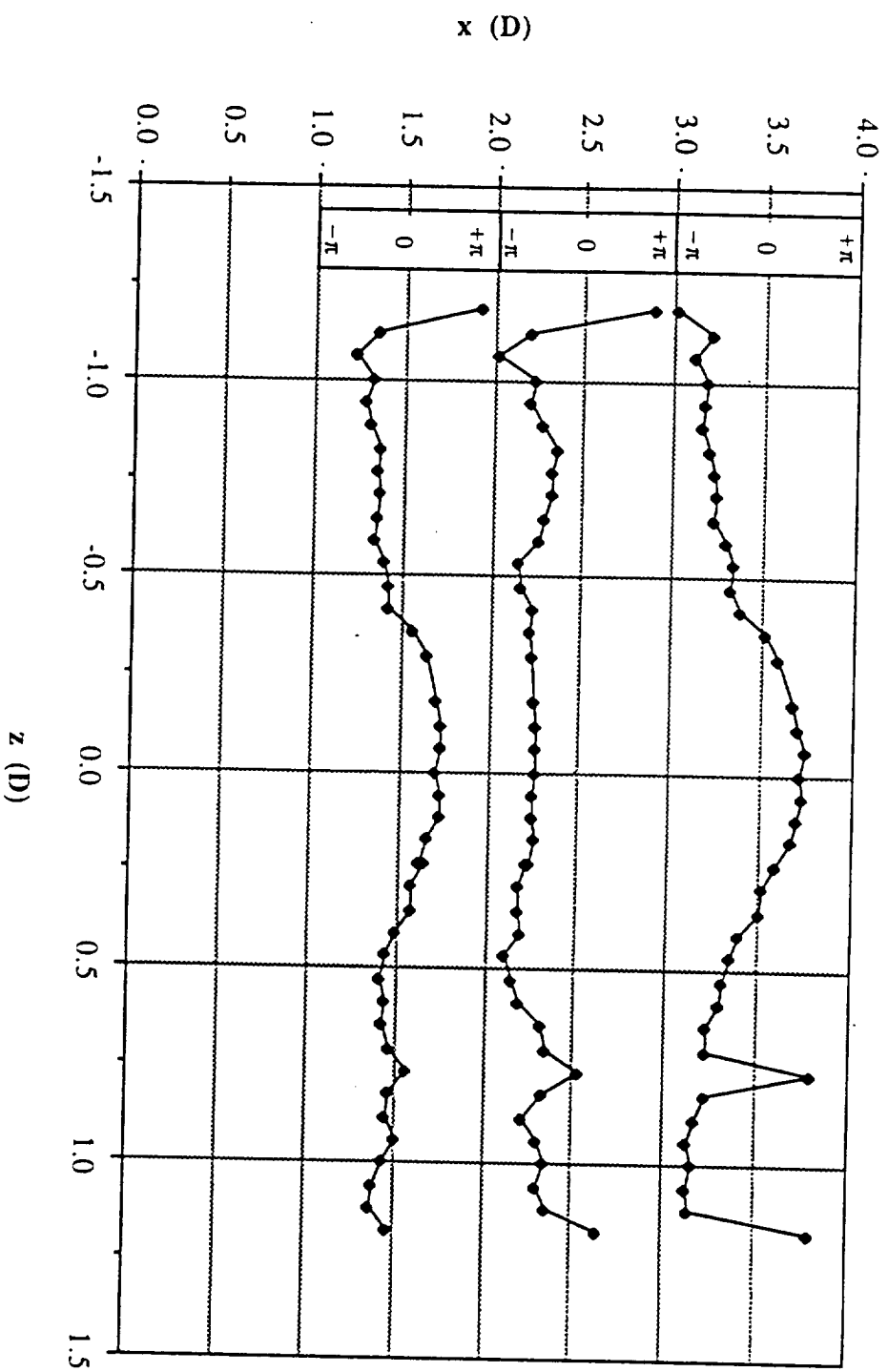


Figure 6.10: Spanwise and streamwise variation of u' phase: 3-D roughness element $12I$ downstream of Branch I; $x = 1.5D$ to $x = 3.5D$; $U(y) = 0.40$; $SPL = 93$ dB.

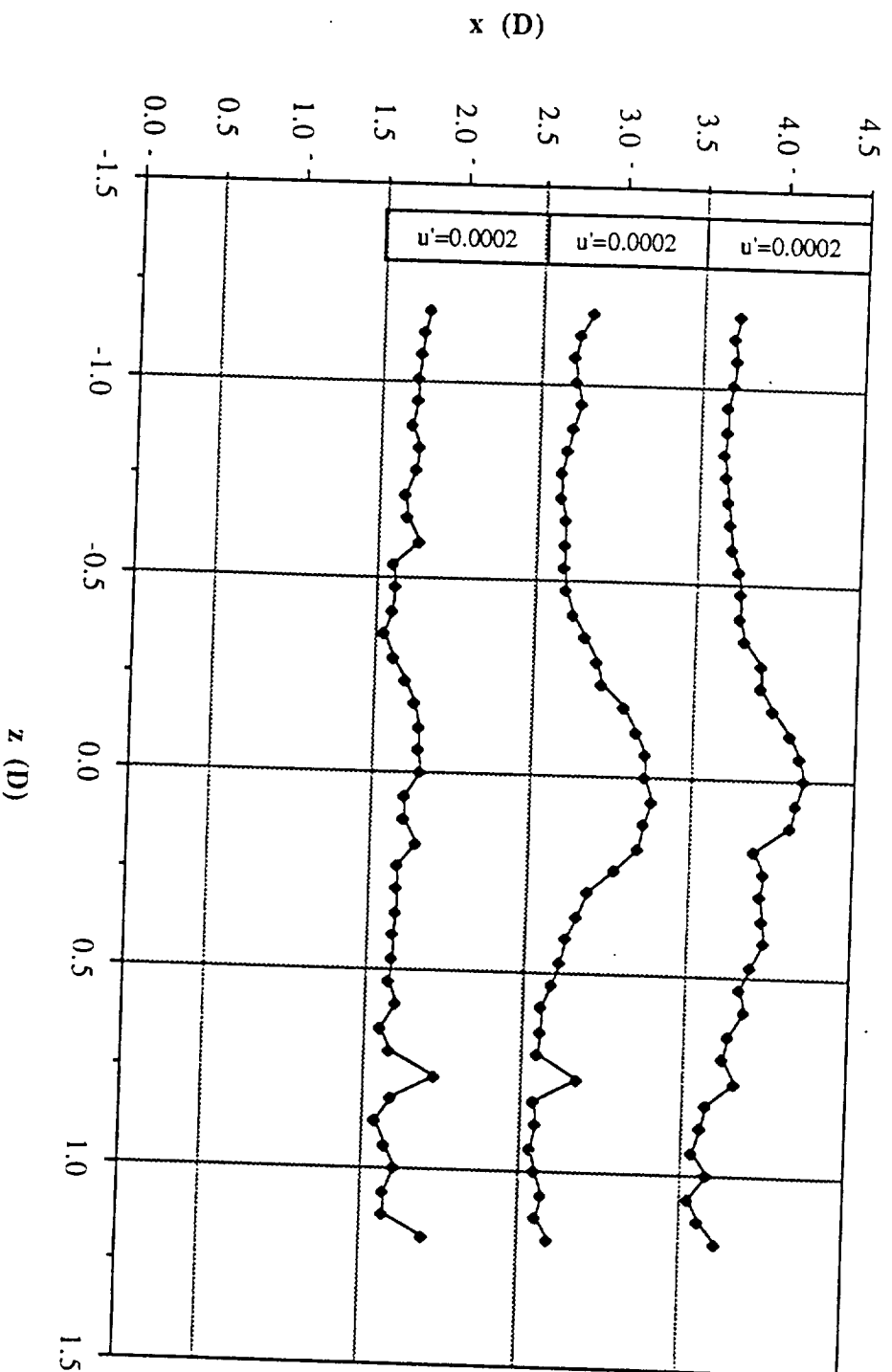


Figure 6.11: Spanwise and streamwise variation of u' amplitude: 3-D roughness element 12D downstream of Branch I; $x = 1.5D$ to $x = 3.5D$; $U(y) = 0.40$; $SPL = 95$ dB.

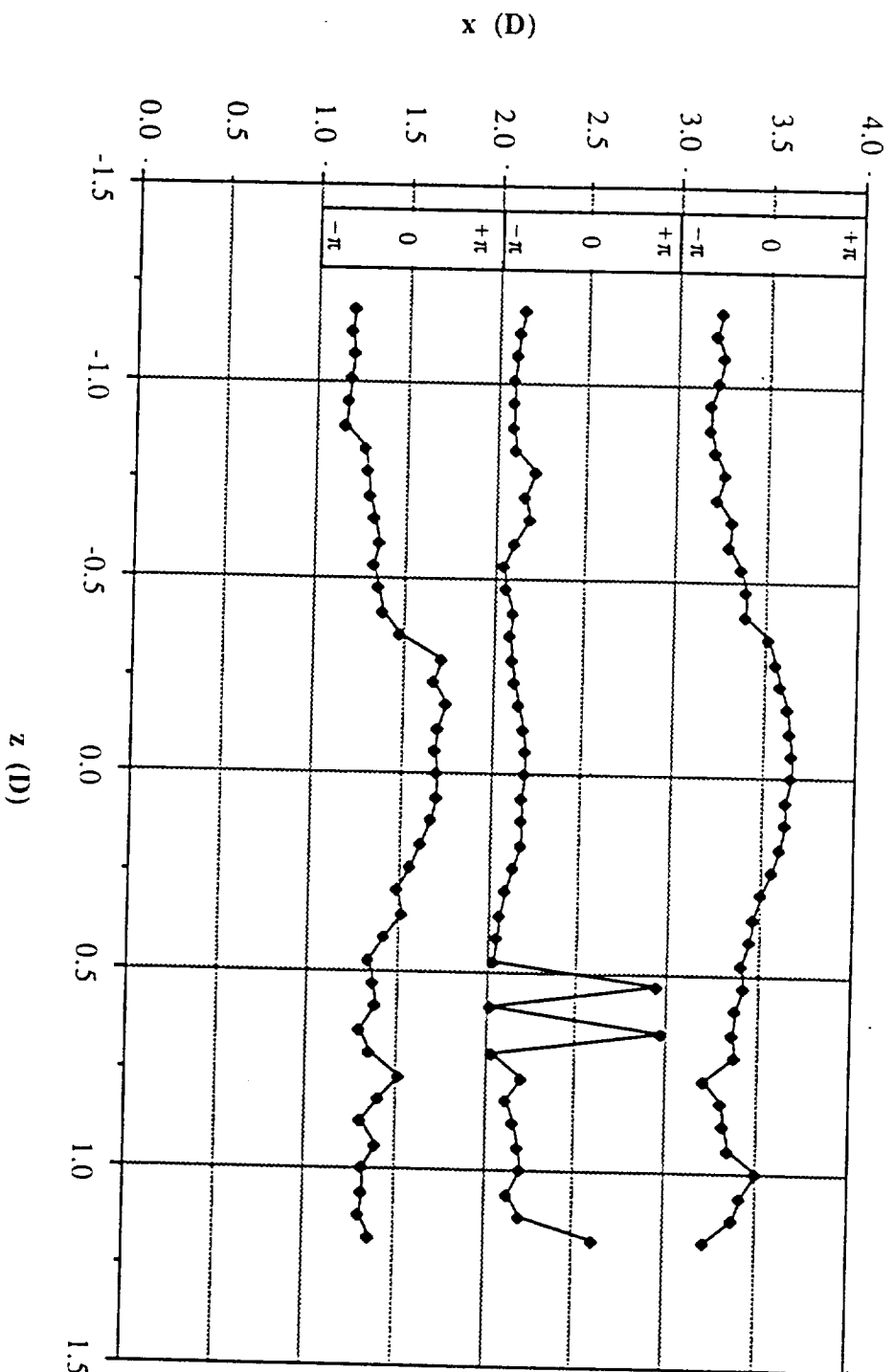


Figure 6.12: Spanwise and streamwise variation of u' phase: 3-D roughness element $12l$ downstream of Branch I; $x = 1.5D$ to $x = 3.5D$; $U(y) = 0.40$; $SPL = 95$ dB.

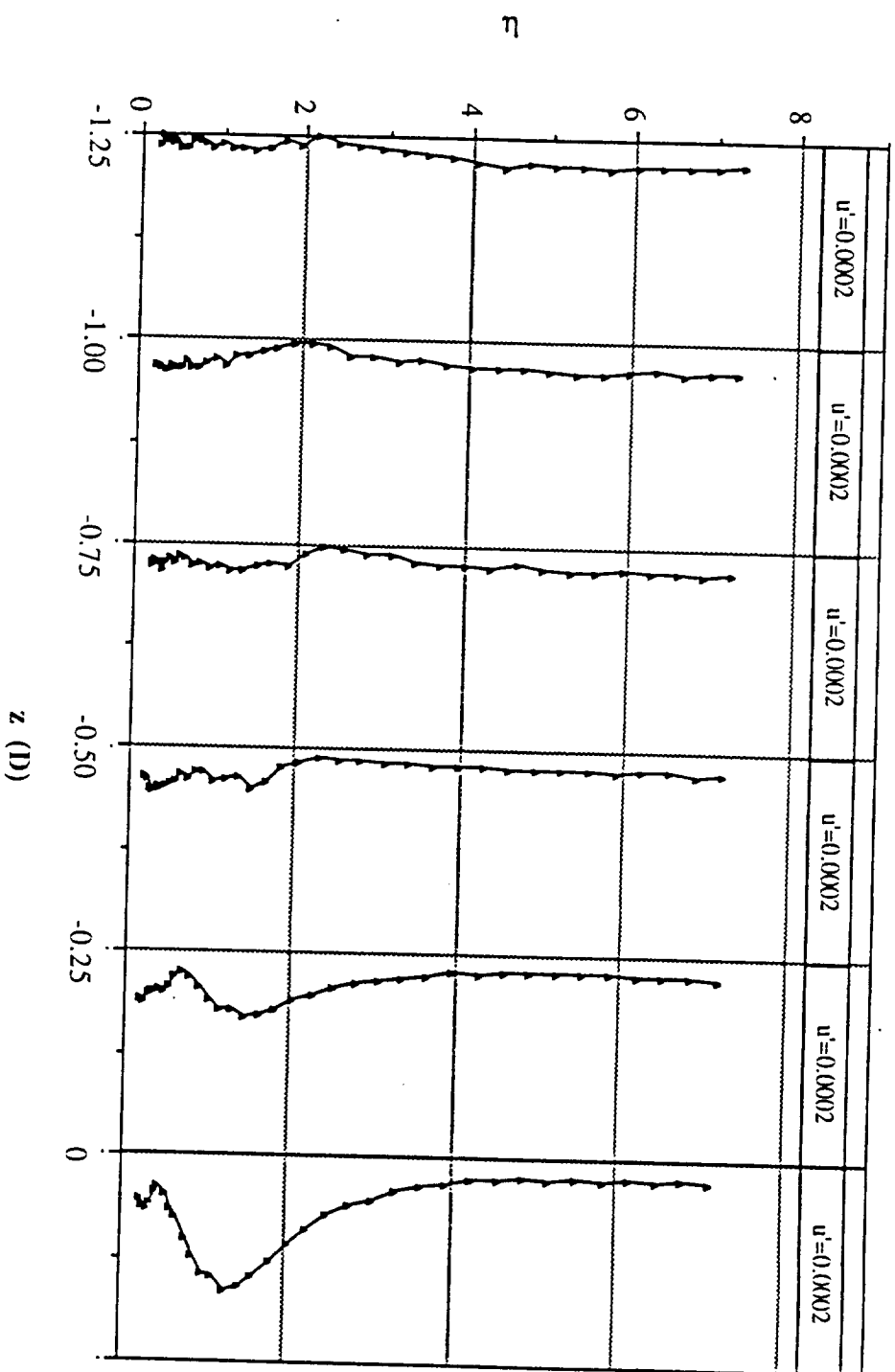


Figure 6.13: Spanwise and normal variation of u' amplitude: 3-D roughness element (2/) downstream of Branch I; $z = -1.25D$ to $z = 0$; $x = 2.5D$; $SPL = 93$ dB.

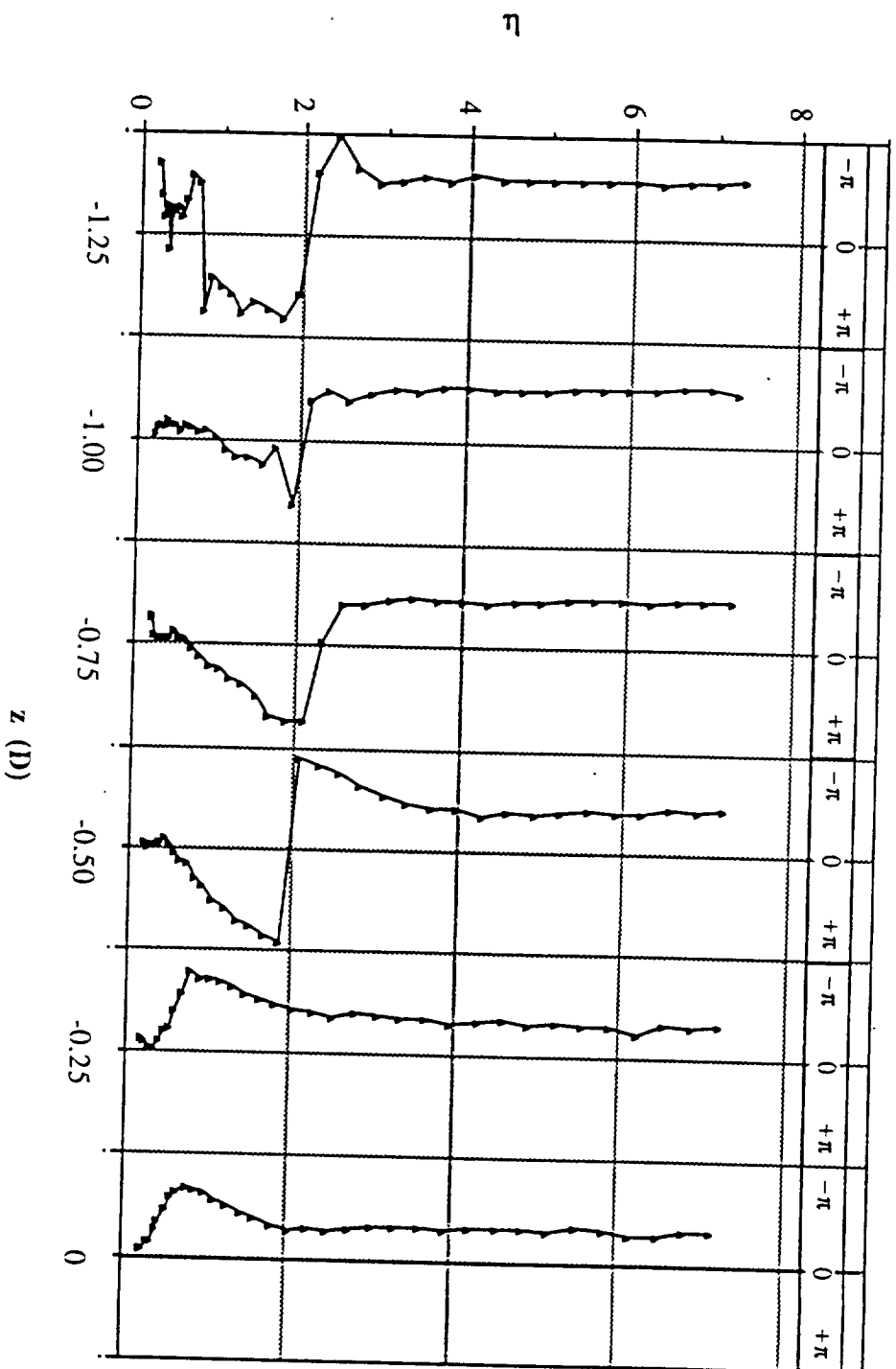


Figure 6.14: Spanwise and normal variation of u' phase: 3-D roughness element (21) downstream of Branch I; $z = -1.25D$ to $z = 0$; $x = 2.5D$; $SPL = 93$ dB.

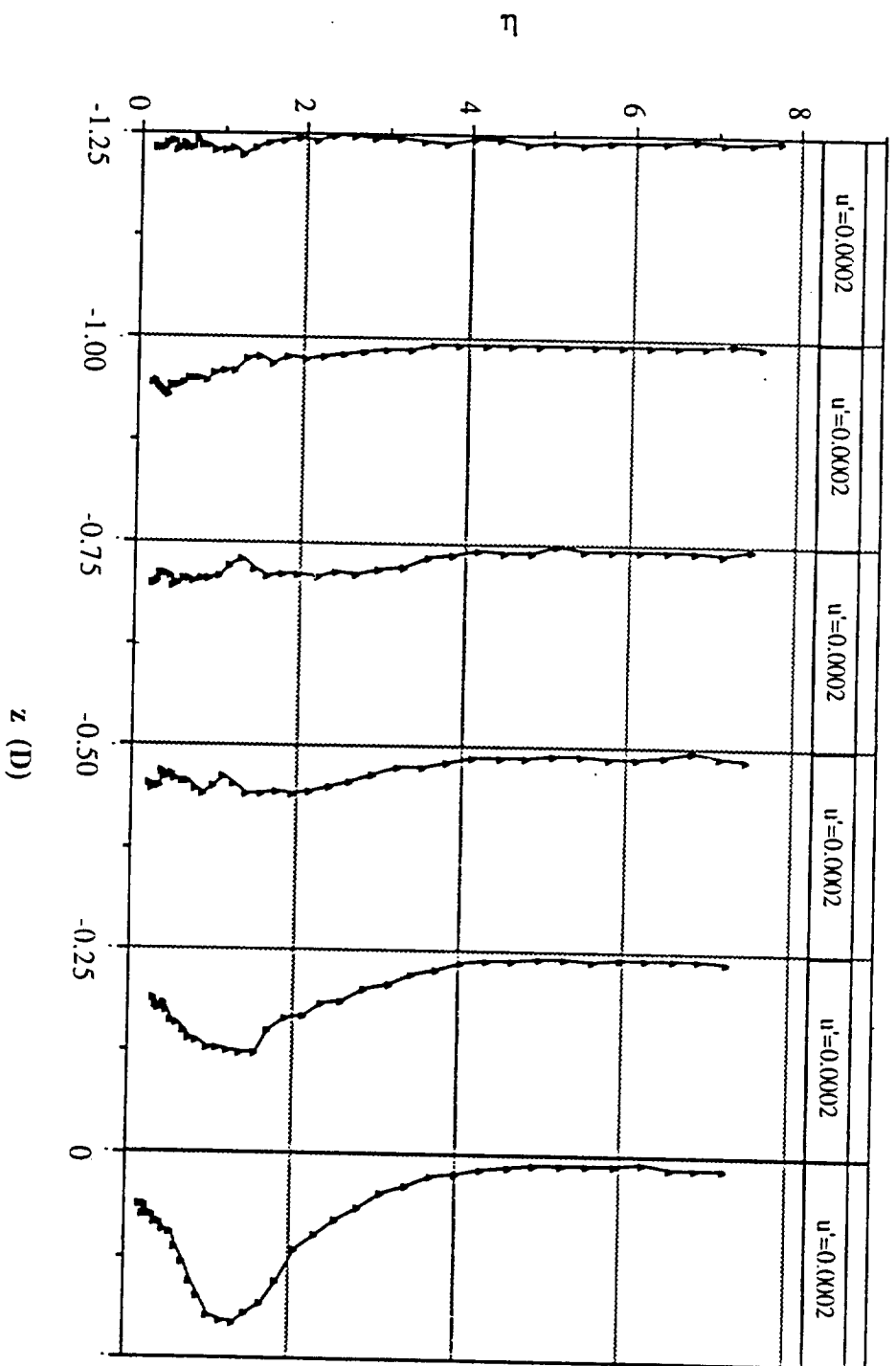


Figure 6.15: Spanwise and normal variation of u' amplitude: 3-D roughness element 12 (l) downstream of Branch I; $z = -1.25D$ to $z = 0$; $x = 2.5D$; $SPL = 95$ dB.

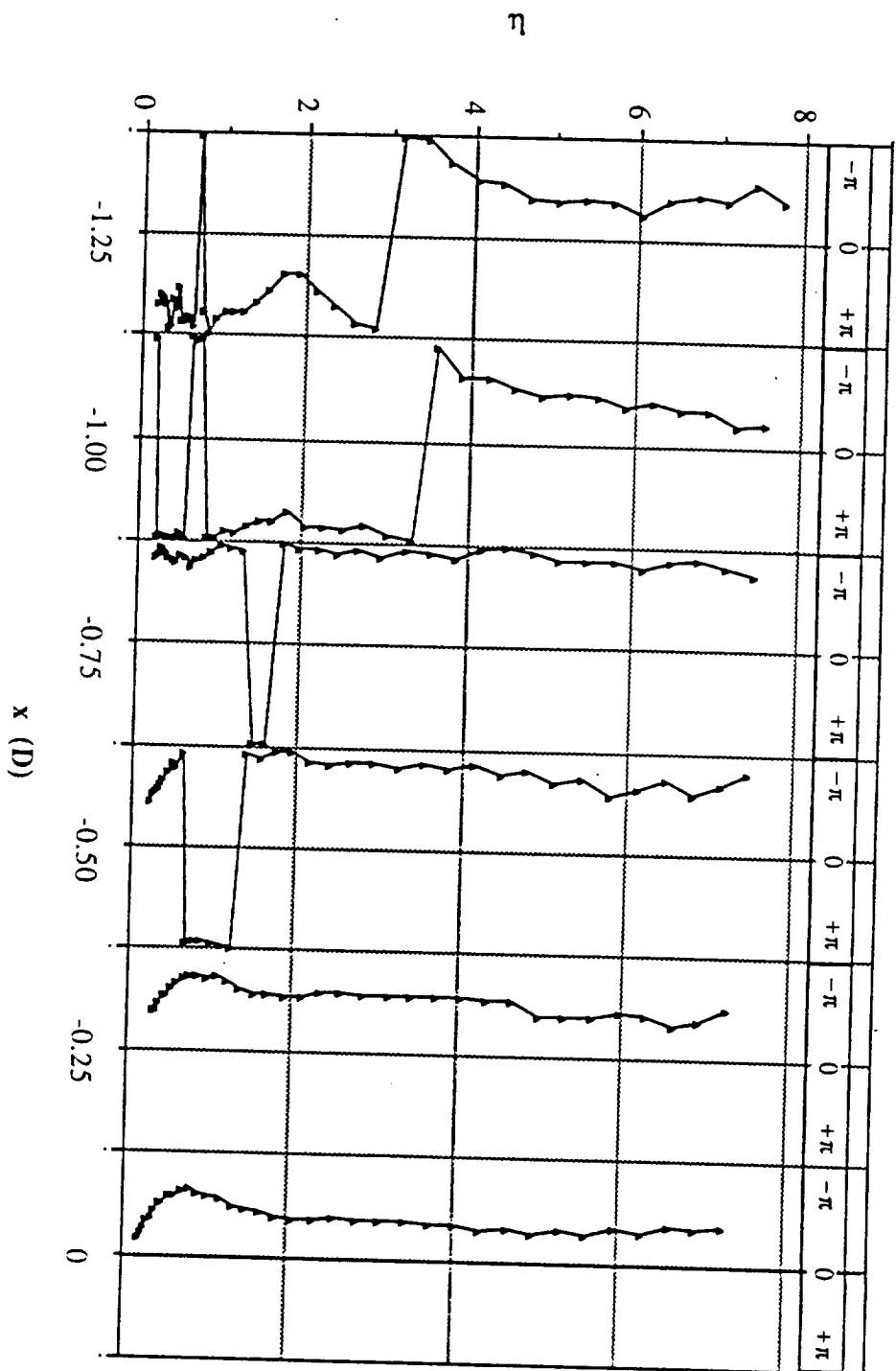


Figure 6.16: Spanwise and normal variation of u' phase: 3-D roughness element (21) downstream of Branch I; $z = -1.25D$ to $z = 0$; $x = 2.5D$; $SPL = 95$ dB.

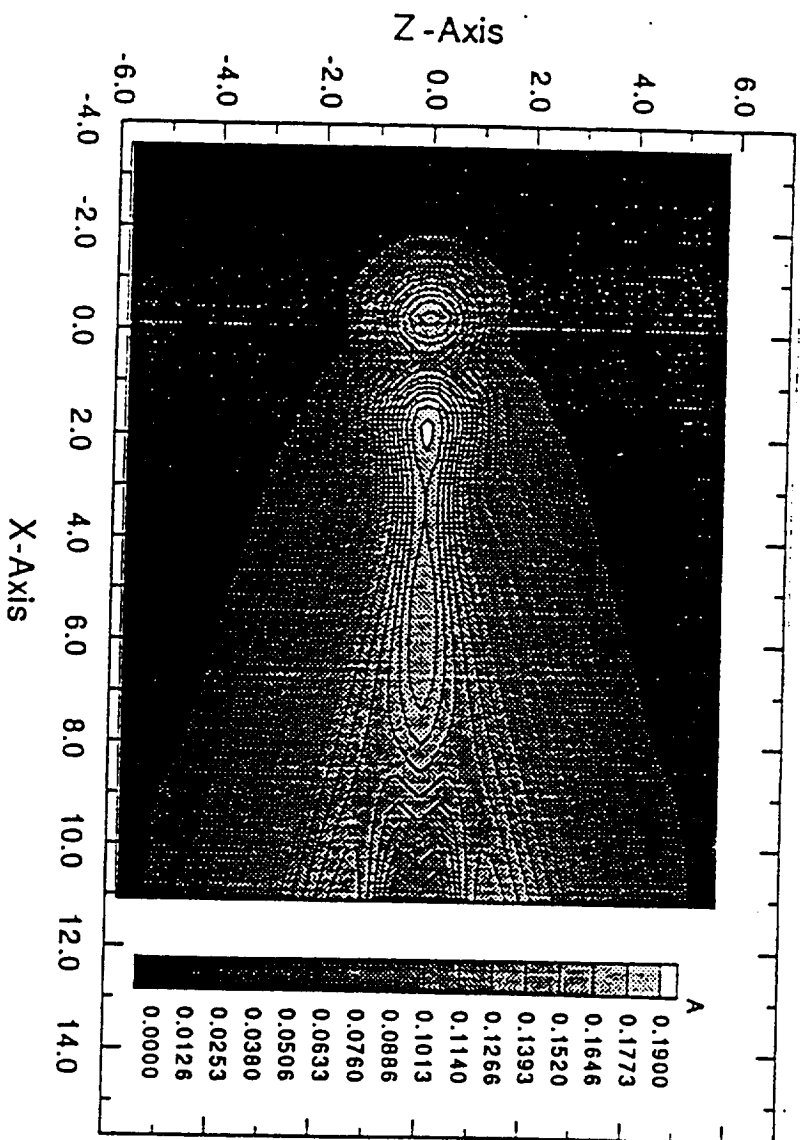


Figure 6.17: Streamwise and spanwise variation of disturbance-velocity amplitude: $S_o = 2.0$, $Y_r = 1.0$. (x and z scaled by $D/2$) (Tadifar, 1990)

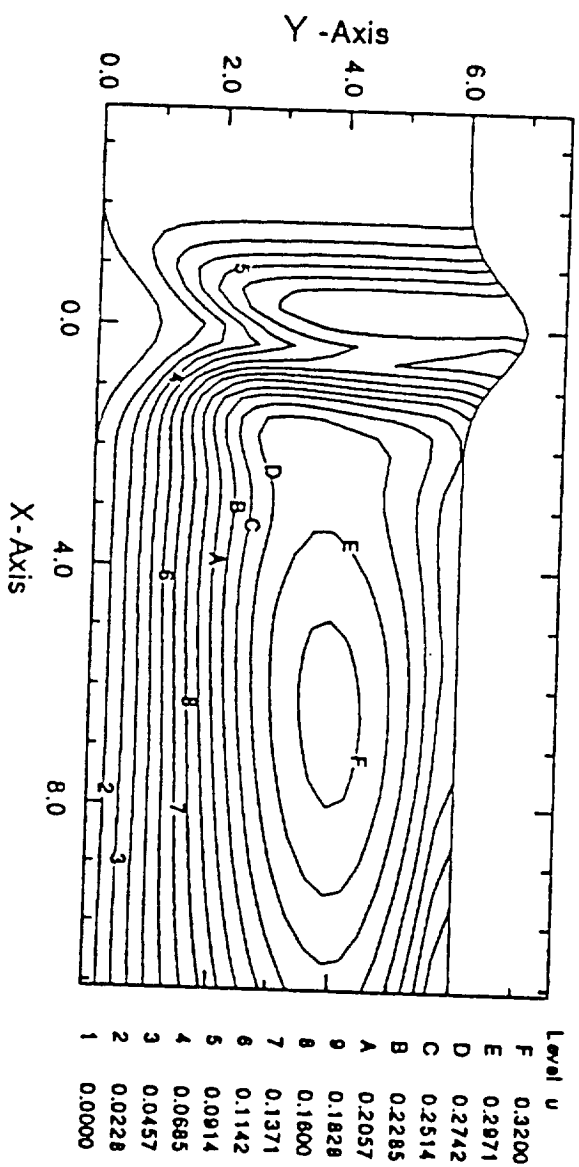


Figure 6.18: Streamwise and normal variation of u' amplitude: $S_o = 2.0$, $Y_r = 1.0$, $z = 0$. (x scaled by $D/2$) (Tadfar, 1990)

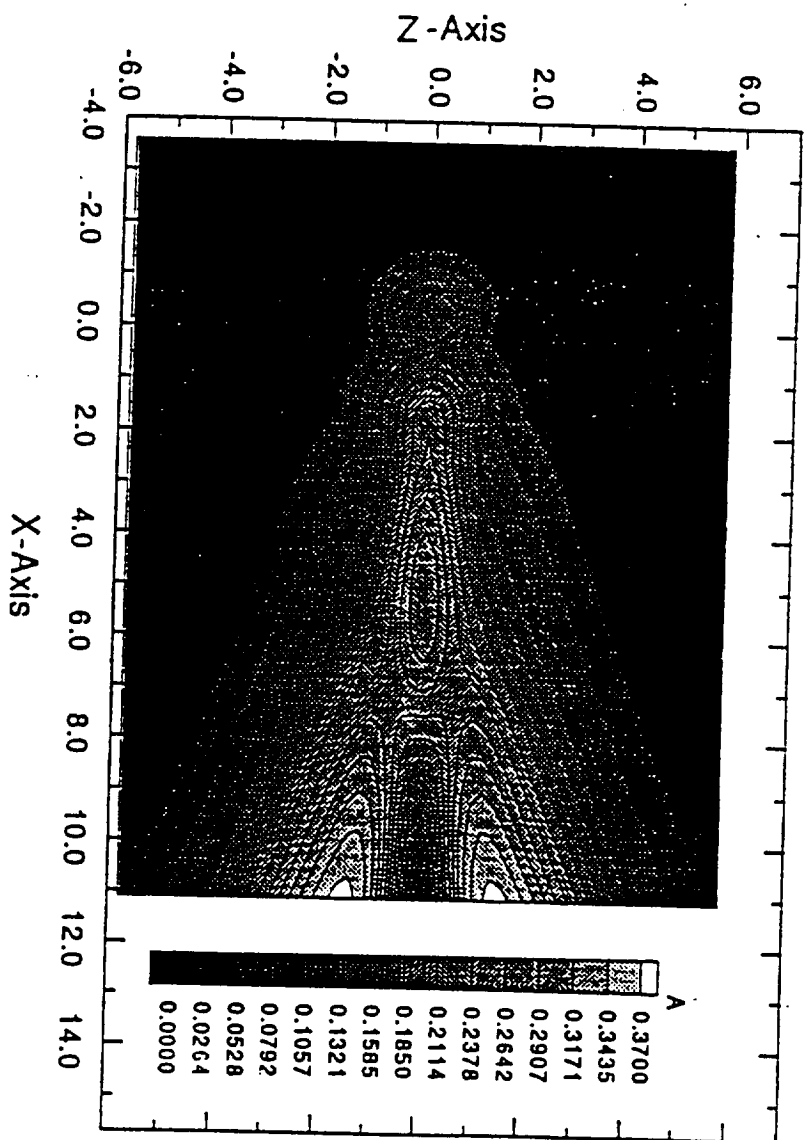


Figure 6.19: Streamwise and spanwise variation of disturbance-velocity amplitude: $S_o = 3.0$, $Y_r = 1.0$. (x and z scaled by $D/2$) (Tadfar, 1990)

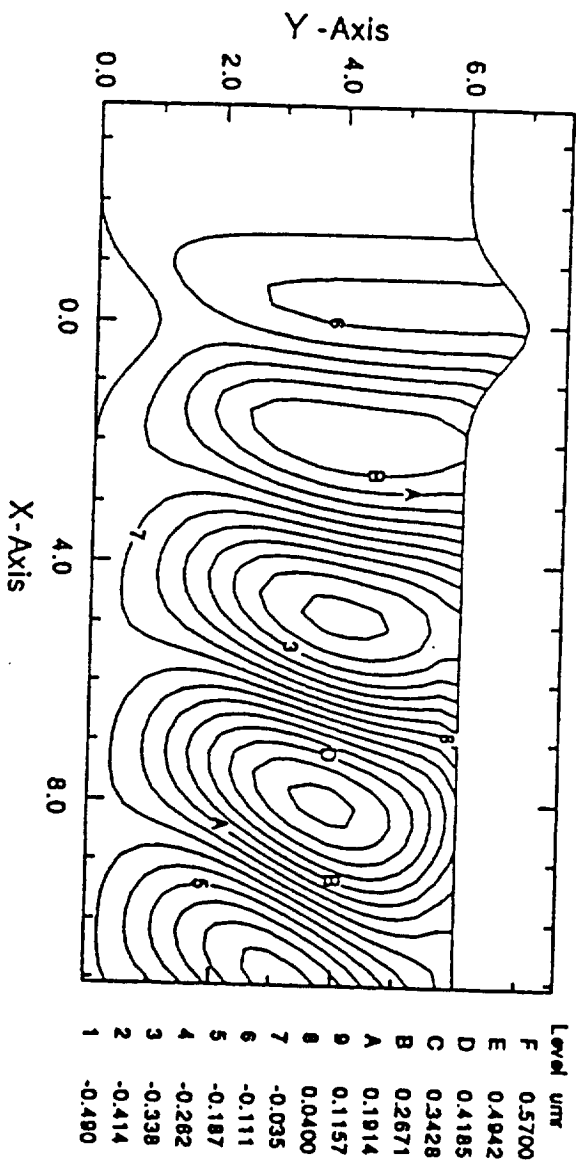


Figure 6.20: Streamwise and normal variation of u' amplitude: $S_o = 3.0$, $\gamma_r = 1.0$, $z = 0$. ($l = \pi/4$, x scaled by $D/2$) (Tadfar, 1990)